Argonne NATIONAL LABORATORY

ANL/LWRS-16/01

Thermal-Mechanical Stress Analysis of PWR Pressure Vessel and Nozzles under Grid Load-Following Mode

Interim Report on the Effect of Cyclic Hardening Material Properties and Pre-existing Cracks on Stress Analysis Results

Nuclear Engineering Division

About Argonne National Laboratory

Argonne is a U.S. Department of Energy laboratory managed by UChicago Argonne, LLC under contract DE-AC02-06CH11357. The Laboratory's main facility is outside Chicago, at 9700 South Cass Avenue, Argonne, Illinois 60439. For information about Argonne and its pioneering science and technology programs, see www.anl.gov.

DOCUMENT AVAILABILITY

Online Access: U.S. Department of Energy (DOE) reports produced after 1991 and a growing number of pre-1991 documents are available free via DOE's SciTech Connect (http://www.osti.gov/scitech/)

Reports not in digital format may be purchased by the public from the National Technical Information Service (NTIS):

U.S. Department of Commerce
National Technical Information Service
5301 Shawnee Rd
Alexandria, VA 22312
www.ntis.gov
Phone: (800) 553-NTIS (6847) or (703) 605-6000
Fax: (703) 605-6900
Email: **orders@ntis.gov**

Reports not in digital format are available to DOE and DOE contractors from the Office of Scientific and Technical Information (OSTI):

U.S. Department of Energy
Office of Scientific and Technical Information
P.O. Box 62
Oak Ridge, TN 37831-0062
www.osti.gov
Phone: (865) 576-8401
Fax: (865) 576-5728
Email: **reports@osti.gov**

Disclaimer

This report was prepared as an account of work sponsored by an agency of the United States Government. Neither the United States Government nor any agency thereof, nor UChicago Argonne, LLC, nor any of their employees or officers, makes any warranty, express or implied, or assumes any legal liability or responsibility for the accuracy, completeness, or usefulness of any information, apparatus, product, or process disclosed, or represents that its use would not infringe privately owned rights. Reference herein to any specific commercial product, process, or service by trade name, trademark, manufacturer, or otherwise, does not necessarily constitute or imply its endorsement, recommendation, or favoring by the United States Government or any agency thereof. The views and opinions of document authors expressed herein do not necessarily state or reflect those of the United States Government or any agency thereof, Argonne National Laboratory, or UChicago Argonne, LLC.

ANL/LWRS-16/01

Thermal-Mechanical Stress Analysis of PWR Pressure Vessel and Nozzles under Grid Load-Following Mode

Interim Report on the Effect of Cyclic Hardening Material Properties and Pre-existing Cracks on Stress Analysis Results

Subhasish Mohanty, William Soppet, Saurin Majumdar, and Ken Natesan

Nuclear Engineering Division, Argonne National Laboratory

March 2016

This page intentionally left blank

ABSTRACT

This report provides an update on an assessment of environmentally assisted fatigue for light water reactor components under extended service conditions. This report is a deliverable under the work package for environmentally assisted fatigue as part of DOE's Light Water Reactor Sustainability Program. In a previous report (September 2015), we presented tensile and fatigue test data and related hardening material properties for 508 low-alloys steel base metal and other reactor metals. In this report, we present thermal-mechanical stress analysis of the reactor pressure vessel and its hot-leg and cold-leg nozzles based on estimated material properties. We also present results from thermal and thermal-mechanical stress analysis under reactor heat-up, cool-down, and grid load-following conditions. Analysis results are given with and without the presence of preexisting cracks in the reactor nozzles (axial or circumferential crack). In addition, results from validation stress analysis based on tensile and fatigue experiments are reported.

This page intentionally left blank

TABLE OF CONTENTS

LIST OF FIGURES

LIST OF TABLES

ABBREVIATIONS

ANL	Argonne National Laboratory
CFD	Computational Fluid Dynamics
CL	Cold Leg
EDF	Électricité de France
EPRI	Electric Power Research Institute
XFEM	Extended Finite Element Method
FE	Finite Element
HL	Hot Leg
ID	Inner Diameter
LAS	Low Alloy Steel
LWRS	Light Water Reactor Sustainability
NPP	Nuclear Power Plant
OD	Outer Diameter
PWR	Pressurized Water Reactor
PWSCC	Primary Water Stress Corrosion Cracking
RCS	Reactor Coolant System
RHR	Residual Heat Removal
RPV	Reactor Pressure Vessel
T-P	Temperature-Pressure

ACKNOWLEDGMENTS

This research was supported through the U.S. Department of Energy's Light Water Reactor Sustainability program under the work package of environmental fatigue study, program manager Dr. Keith Leonard.

This page intentionally left blank

1 Introduction

Use of renewable energy such as solar and wind has increasingly become a worldwide goal to avoid catastrophic climate change. Widespread availability of clean, affordable, and reliable energy would also be a cornerstone of the world's increasing prosperity and economic growth [1]. However, such renewable energy sources are only intermittently available and cannot reliably be used for base-load demand.

In many countries such as the U.S., France, South Korea, and Japan, nuclear energy is extensively used as a base-load source of electricity. However, when more and more renewable energy sources are connected to the electric grid, a question arises: do the nuclear power plants (NPPs) have the ability to adjust to a varying load from the interconnected grid, including daily and seasonal variations [2-10]? Under the load-following mode, the pressure boundary components of NPPs may be subjected to additional thermal-mechanical cycles, particularly when the fluctuation in the gap between the grid demand and renewable energy supply is severe (in terms of both frequency and amplitude). Although most modern nuclear plants are designed to follow grid demands to a certain extent through consideration of a large safety factor, no study (at least none reported in the open literature) has been undertaken to determine the stress-strain state of reactor components under grid-load following. Most previous research on NPP component safety assessment, including our own [11-12], is based on a stress analysis of components using simplified design transients. For accurate structural integrity assessment of NPP components, it is necessary to perform structural fatigue evaluation under more realistic loads [13-15]. In this regard, thermal-mechanical stress analysis of NPP components under the grid load-following mode might be necessary for accurate fatigue evaluation. In addition, since there are plans for increasing the life of current NPPs from their original design life of 40 years to the extended life of 80 years, aging-related material issues [16,17] can play additional detrimental role in the structural integrity of NPP components.

Argonne National Laboratory (ANL), under the sponsorship of the Department of Energy's Light Water Reactor Sustainability (LWRS) program, has been involved with extensive material testing [18,19] and mechanistic modeling [11,12] for assessing the structural integrity of NPP components under design and extended service conditions. In this report we present detailed results from thermal mechanical stress analysis of a reactor pressure vessel (RPV) and its nozzle (both with and without preexisting axial/circumferential cracks) under typical reactor heat-up, cool-down, and load-following modes. This work is a continuation of an LWRS environmental fatigue program.

This report is organized into the following sections:

1. Finite Element Model of Reactor Pressure Vessel and Nozzles
2. Temperature-Pressure Boundary Conditions under Heat-Up, Cool-Down, and Grid Load Following
3. Heat Transfer Analysis of RPV and Nozzles
4. Material Properties for Structural Analysis
5. Stress Analysis of Laboratory Specimens under Isothermal Fatigue Loading
6. Thermal-Mechanical Stress Analysis of RPV and Nozzles without Preexisting Cracks
7. XFEM Modeling and Thermal-Mechanical Stress Analysis of RPV and Nozzles with Preexisting Cracks
8. Summary and Future Work

2 Finite Element Model of Reactor Pressure Vessel and Nozzles

We developed finite element (FE) models for both heat transfer analysis and for subsequent thermal-mechanical stress analysis. In our earlier work [11, 12] we presented a preliminary/skeletal FE model of an overall reactor consisting of a reactor pressure vessel, hot leg, cold leg, and steam generator. In this work, we present a detailed FE model of the reactor pressure vessel and its nozzle only. The major aim was to perform a stress analysis under realistic thermal-mechanical loading and to study the stress-strain state of the RPV and its nozzles with/without the presence of crack. The details of the FE model are discussed below.

The models were developed by using commercially available ABAQUS FE software [20]. The FE models are based on approximate geometry determined from publicly available literature [16, 21-24]. The RPV model includes a typical two-loop pressurized water reactor with two hot-leg (HL) nozzles and 4 cold-leg (CL) nozzles. Figure 2.1 shows the outer/inner diameter (OD/ID) surface of the RPV and its HL and CL nozzles. For the requirement of modeling cracks (discussed in Section 8), 3D models were developed and meshed by using eight noded 3D brick elements. In our previous work [11, 12] we found that eight-node linear elements (DC3D8) were sufficient to model heat transfer compared to a computationally expensive counterpart of 20-node brick elements (DC3D10). For stress analysis, the corresponding C3D8, 8-node linear elements were used. Note that in our earlier work [11, 12], we considered other components such as the HL, CL, and steam generator; in the present work, however, we have not considered those components to reduce the computational burden by limiting the number of finite elements. Instead, we included HL/CL nozzles and increased the number of elements along the thickness direction to allow modeling of preexisting cracks. Figure 2.2 shows the OD and ID surface of the RPV and it nozzle FE mesh. A finer mesh was selected near the nozzle area for modeling possible stress hot spots arising due to the presence of openings, such as nozzles and preexisting cracks. Figure 2.3 shows the magnified geometry model and FE mesh near the RPV nozzle locations. The RPV and nozzle assembly have a total of 72,977 DC3D8 elements for heat transfer models or C3D8 elements for structural analysis models. Table 2.1 shows the number of elements associated with individual components. The materials properties of 508 low alloy steel (508 LAS) is used for the FE modeling of all the sections of the RPV and its nozzles.

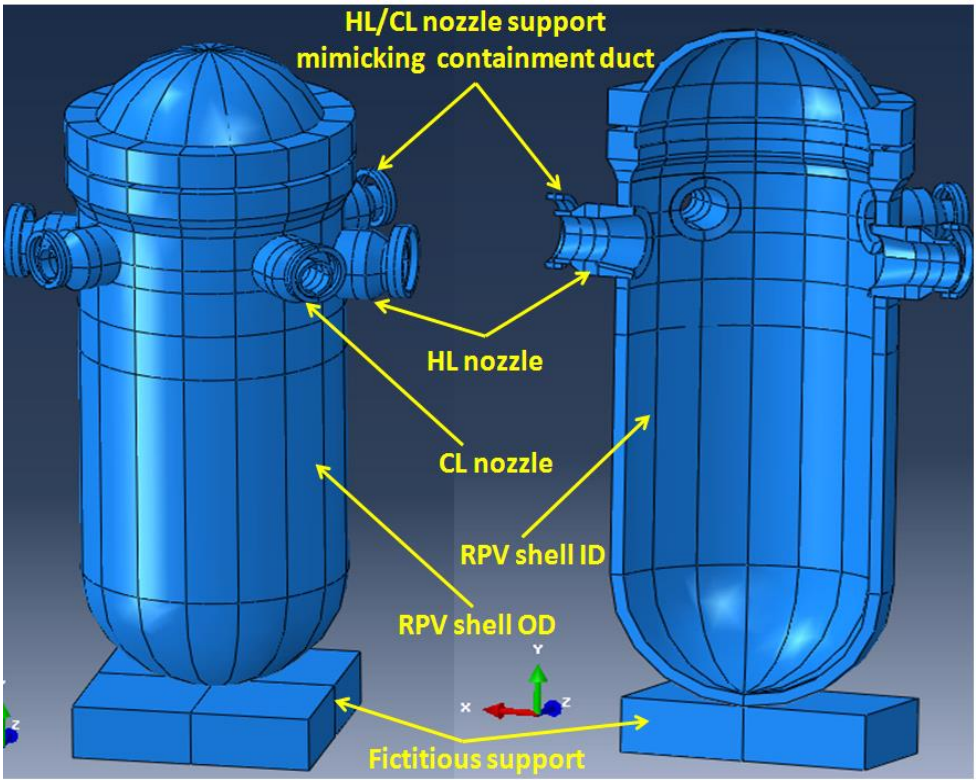

Figure 2.1 Solid model of RPV and its nozzle.

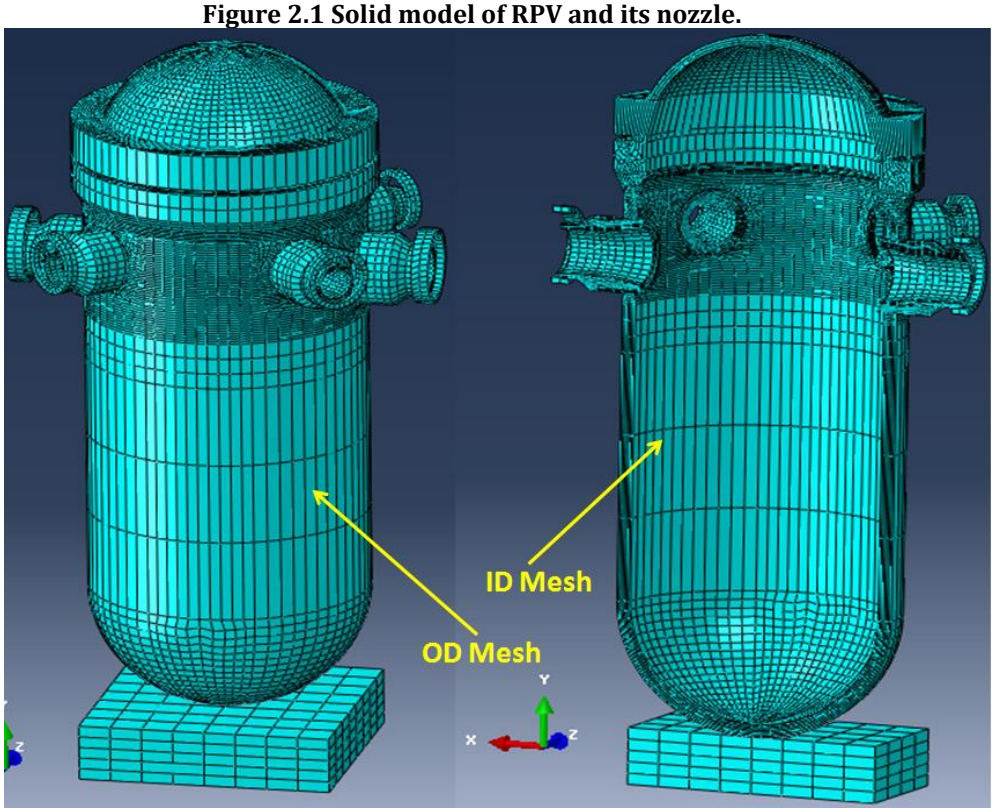

Figure 2.2 RPV and its nozzle FE mesh.

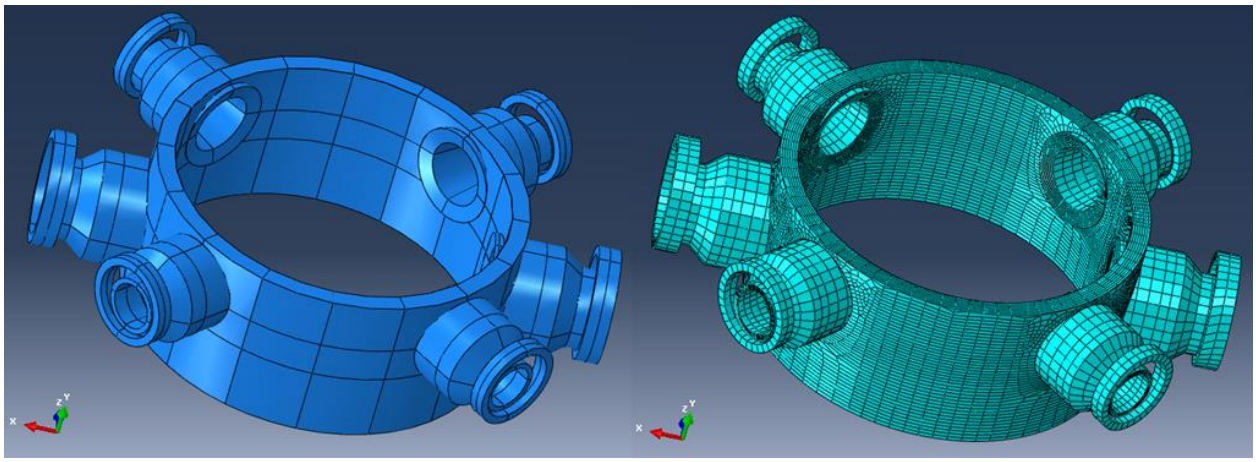

Figure 2.3 Solid model and FE mesh near the nozzle area.

Table 2.1 Number of finite elements in RPV and its nozzle model.

Component Name	Number of components	Material Type	Number of finite elements
Pressure vessel	1	508 LAS	51,021
Hot leg nozzle	2	508 LAS	2x5012 = 10,024
Cold leg pipe	4	508 LAS	4x2800=11,200
RPV base plate	1	508 LAS	320
HL nozzle support duct	2	Artificial large stiffness material	2x78=156
CL nozzle support duct	2	Artificial large stiffness material	4x64=256
Total number of elements in assembly			72,977

The bottom section of the RPV was tied to a thick base plate, which was attached to the ground and constrained in all directions. In contrast, the HL/CL nozzles were supported through circular supports that mimic the duct in the RPV cavity or containment structure. In the FE model, contact boundary conditions were selected between the ID surface of these circular supports and OD surface of nozzles. This condition was designed to mimic the real reactor conditions, allowing free thermal expansion of the nozzle in all three directions. However, note that the above boundary conditions are simplified assumptions and do not necessarily represent the exact boundary conditions in a real reactor. In addition, in the present assembly-level model, we did not consider the plane of symmetries because to model crack in one of the HL nozzles. In addition to modeling the reactor temperature and pressure cycle, the dead load associated with reactor coolant water and the self-weight of RPV and its nozzles were considered for the stress analysis models. In addition, a typical RPV is subjected to substantial gravity load associated with the reactor internals.

The approximate loads due to these internals are also included in the FE model as additional gravity load. Based on the data given in reference [25], in the discussed model, the upper and lower internal weights were considered as 50,000 kg and 120,000 kg, respectively. From the FE model, the volume of the RPV and nozzle was estimated as 37.6 m^3. Assuming 50% of this volume is occupied with reactor coolant water, the weight of the coolant water was estimated to be 18,800 kg. Using ABAQUS, we performed a frequency/modal analysis to estimate the self-weight of the RPV and its nozzles. This parameter was estimated as 325,663 kg. The total dead weight (including self-weight of RPV and internals and weight due to coolant) was estimated to be 514,463 kg. This total weight was modeled as distributed gravity load, with an artificial gravity constant ($g_{artificial}$) estimated through the following relation:

$$g_{artificial} = \frac{mass_{self}}{mass_{total}} g_{actual} = \frac{514,463}{325,663} 9.81 = 15.497 \text{ m/sec}^2.$$

3 Temperature-Pressure Boundary Conditions under Heat-Up, Cool-Down, and Grid-Load Following

The heat transfer and structural analysis requires an appropriate temperature and pressure (T-P) boundary condition as input to the FE model. These inputs can be obtained through performing system-level thermal-hydraulic and computational fluid dynamics (CFD) analysis. Performing system-level thermal-hydraulic and CFD analysis is highly complex, computationally intensive, and not the major focus of our work. Hence, we used an approximate T-P boundary condition estimated based on literature data. In the present work we considered one reactor operation cycle comprising heat-up, normal operation under grid load following, and cool-down conditions. The estimation of associated T-P boundary conditions is briefly described below.

3.1 Reactor Heat-up and Cool-down

According to the Westinghouse NPP manual [26], the heat-up and cool-down operations are conducted in a series of steps for safe operation of the reactor. According this manual, for a typical NPP, some of the important steps followed during heat-up are:

A) Cold shutdown initial condition:

- Ideally, maintain the reactor coolant system (RCS) temperature between 150 ^{o}F (65.5 ^{o}C) and 160 ^{o}F (71.1 ^{o}C). The temperature could be lower depending on the decay heat load from the reactor core. At this condition, the RCS pressure is maintained at 100 psig (0.689 MPa).

B) Heat-up condition from cold shutdown to hot shutdown:

- Begin heating up the pressurizer to increase RCS pressure. The heat-up rate cannot exceed 100 ^{o}F (37.8 ^{o}C) per hour for both RCS and pressurizer heat-up.
- Maintain RCS temperature below 160 ^{o}F (71.1 ^{o}C) by regulating the flow through the residual heat removal (RHR) system.
- Open the main steam-line isolation valve.
- Continue pressurizer heating up to 430 ^{o}F (221.1 ^{o}C). At this point the RCS pressure would be approximately 325 psig (2.24 MPa).
- Stop RTR.
- Allow RCS temperature to increase to 200 ^{o}F (93.3 ^{o}C)

C) Heat-up from hot shutdown to hot standby condition:

- Allow the RCS pressure to increase.
- Before the RCS pressure reaches 1000 psig (6.895 MPa), open isolation valve of each of the cold leg accumulators.
- Increase RCS pressure to 2235 psig (15.41 MPa) and set RCS pressure control mode as automatic to maintain that pressure.

- Maintain the hot standby condition of RCS at a temperature between 540 ^{o}F (282.2 ^{o}C) and 547 ^{o}F (286.1 ^{o}C).

Once the hot standby condition is reached, the reactor has to undergo the power operation mode by withdrawing the control rods. For refueling and maintenance, the reactor has to be brought from the full power mode to cold shutdown by following a similar reverse strategy as the heat-up procedures.

For realistic stress analysis, it is essential to use the prototypical T-P boundary condition as discussed above. In the present work we use the heat-up and cool-down T-P profile given by the Electric Power Research Institute (EPRI) [27]. The respective temperature and pressure profiles based on EPRI literature are shown in Figures 3.1 and 3.2. The EPRI heat-up and cool-down procedures are along a similar line to the above discussed Westinghouse procedures. Similar T-P profiles are also used for the Électricité de France (EDF) reactor heat-up and cool-down [28].

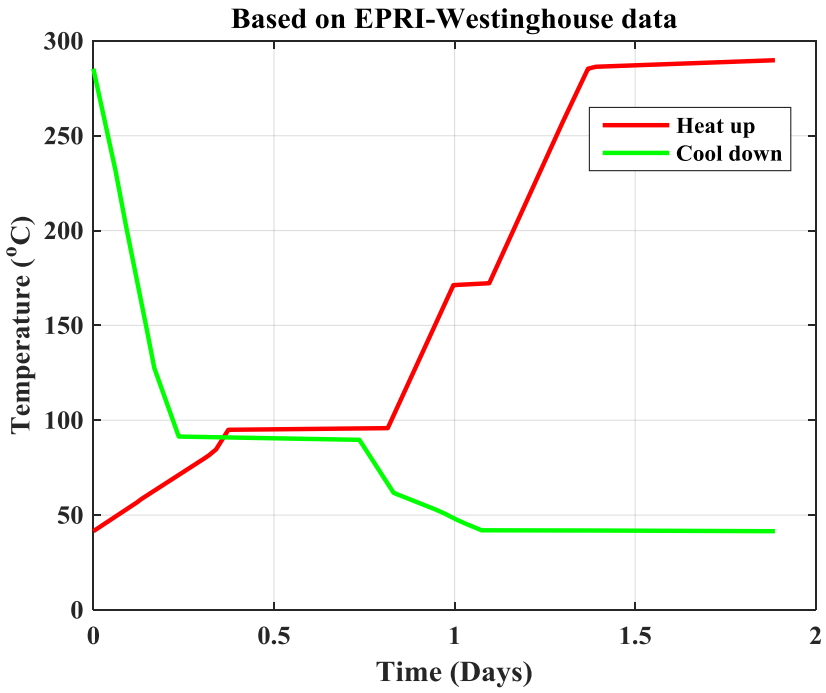

Figure 3.1 Temperature profile during reactor heat-up and cool-down [27].

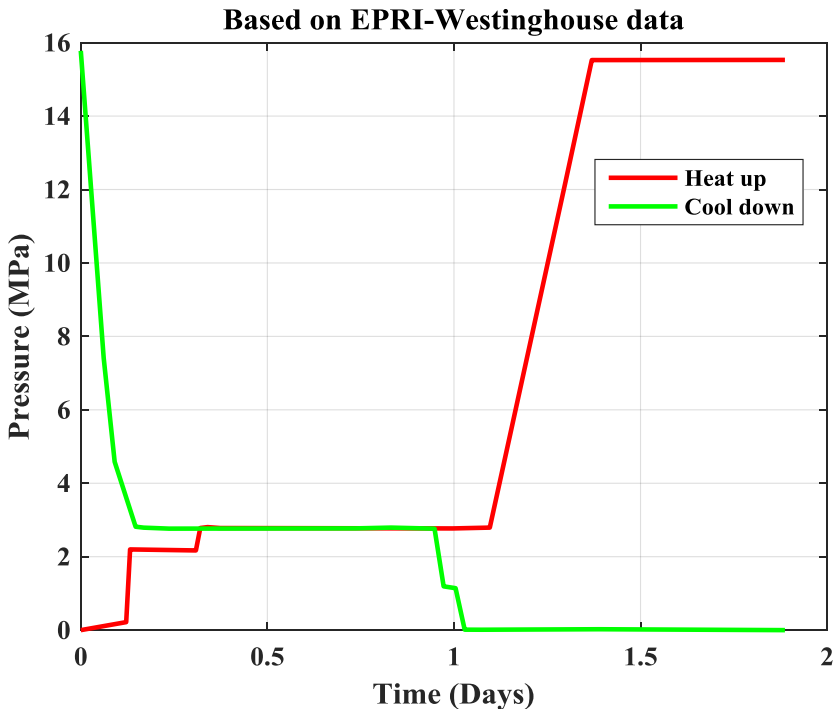

Figure 3.2 Pressure profile during reactor heat-up and cool-down [27].

3.2 Reactor Power Operation under Load Following

After hot standby, the reactor is powered up by following a procedure to reach its rated or maximum operating power. Although the absolute value of the rated or maximum operating power varies from reactor to reactor, it is not expected that the reactor would operate under a perfect steady-state condition. Under a realistic scenario the reactor power would fluctuate, depending on the grid demand. Hence, it is essential to incorporate these power fluctuations and associated temperature-pressure variation in the FE model of a reactor component for accurate evaluation of its stress-strain state. In the present work the power-following condition of an EDF pressurized water reactor is considered.

The power-following time plot for a typical EDF reactor operation cycle can be found from references (refer Figure 1 of [2] or Figure E.1 of [3]). The given history in those reference has hundreds of peaks (both small and large). Modeling all these peaks in the FE model is time consuming and unnecessary. Hence, only approximately 300 representative peaks were considered from the original EDF power-following time data. Figure 3.3 shows the simplified percentage power time plot considered for the present FE model. The literature [2, 3] also gives approximate temperature variations in the HL and CL of an EDF reactor with respect to percentage power. Figure 3.4 shows the temperature relation with respect to percentage power. Using the percentage power history shown in Figure 3.3 and power versus temperature relation shown in Figure 3.4, we estimated the approximate temperature history in the HL and CL during power operation. Figure 3.5 shows the estimated temperature histories. In addition to the temperature history during power operation, for FE models, we also need the temperature boundary condition during heat-up and cool-down conditions. To that end, the heat-up and cool-down history shown in Figure 3.1 was combined with the temperature history shown in Figure 3.5 to estimate the HL and CL temperature

history under a single loading cycle comprising a heat-up, power operation, and cool-down sequence. Note that during the heat-up and cool-down procedure, it is assumed that the CL and HL follow the same temperature-time plot. Figure 3.6 shows the estimated temperature for the HL and CL over the entire reactor loading cycle. This temperature history was used in the discussed FE model as the temperature boundary condition. The HL temperature history was used to model the ID surface temperature of the HL nozzles, whereas the CL temperature history was used to model the ID surface temperature of the CL nozzles. The temperature of the ID surface of the RPV was assumed to be similar to that of the CL. Similar to the full-cycle temperature history, a full-cycle pressure history was estimated to model the ID surface pressure boundary condition of the RPV, HL, and CL. Unlike the temperature history during power operation, the pressure was assumed to be fixed and equal to the hot standby condition. Figure 3.7 shows the estimated combined pressure history during a complete reactor loading cycle. This pressure history was used to model the ID surface pressure boundary condition of the HL, CL, and RPV.

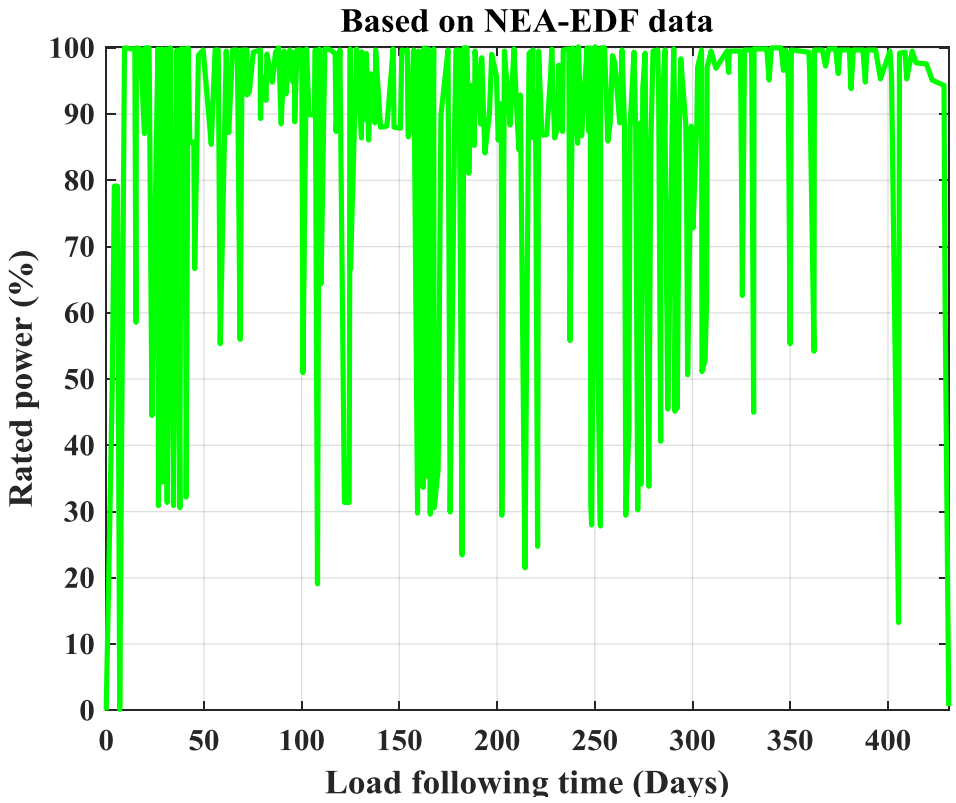

Figure 3. 3 Simplified percentage power history considered for present FE model.

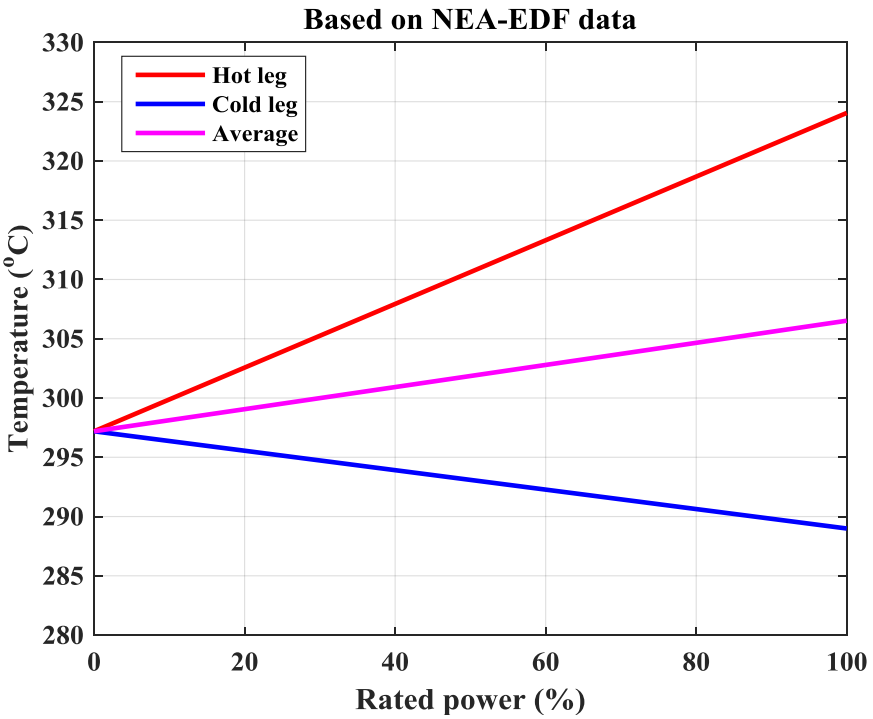

Figure 3.4 Temperature relations with respect to percentage power in EDF reactor [3].

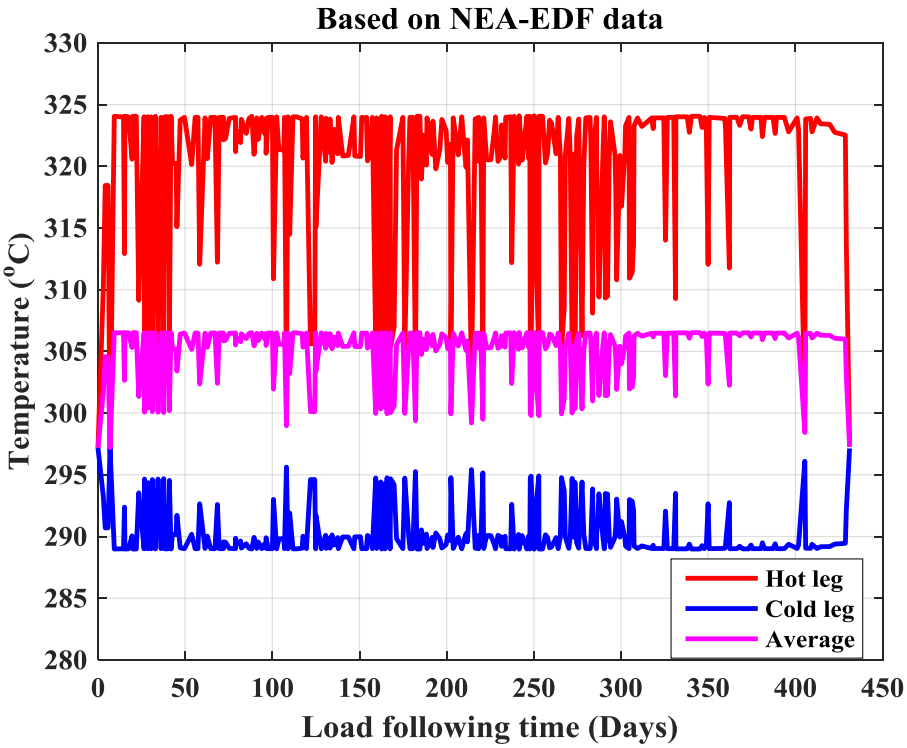

Figure 3.5 Approximate estimated temperature histories in HL and CL and their average during normal power operation under grid-following mode.

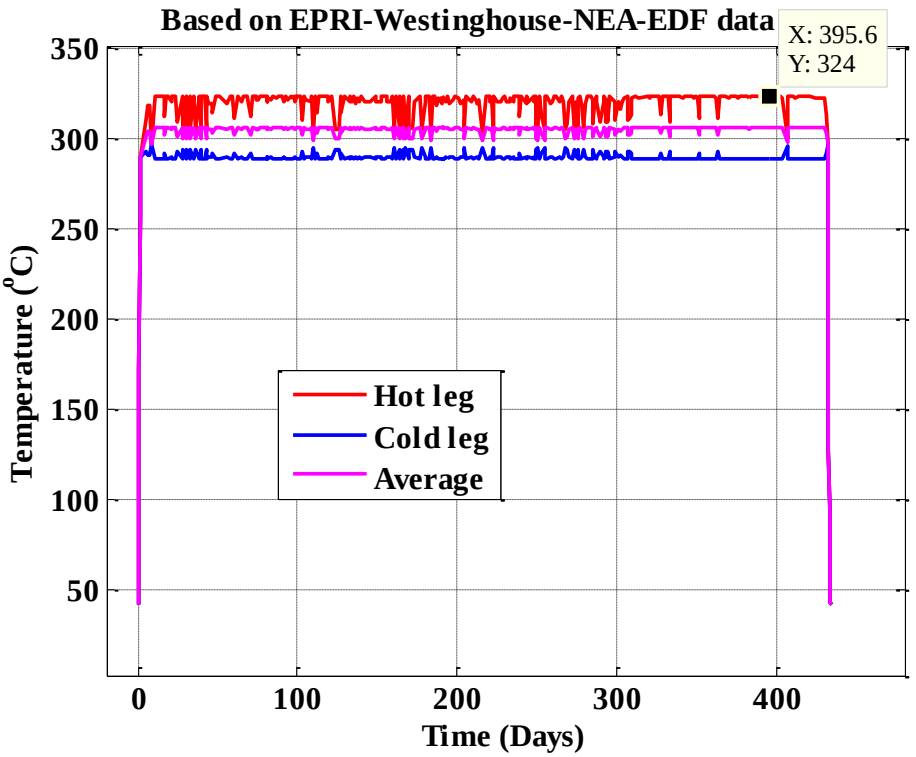

Figure 3.6 Estimated temperature for HL and CL over entire reactor loading cycle.

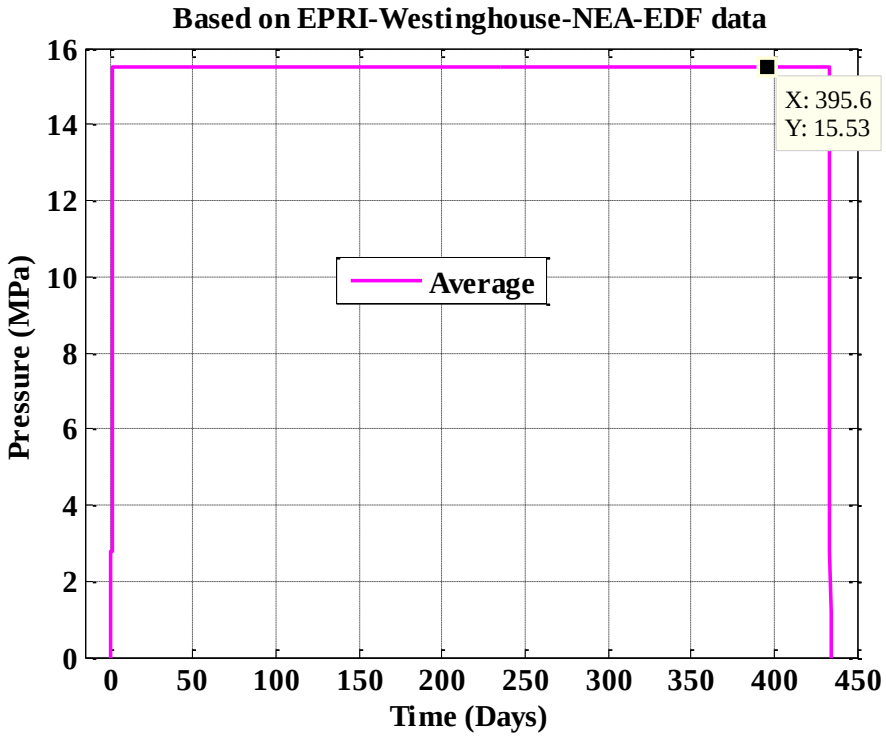

Figure 3.7 Estimated combined pressure history during complete reactor loading cycle.

4 Heat Transfer Analysis of RPV and Nozzles

Using the FE model discussed in section 2, we performed a heat transfer analysis for a RPV. The analysis was performed to estimate nodal temperature across the RPV and HL/CL nozzle thickness. These data can then be used for the thermal-structural stress analysis. The related thermal material properties and analysis results are summarized below.

4.1 Thermal Material Properties

To model heat transfer from the reactor coolant water to reactor metal, we estimated an approximate heat transfer coefficient (h) using the following relation:

$$N_u = \frac{hD_e}{k_w} \tag{4.1}$$

where D_e is the hydraulic diameter (assumed equal to the diameter of the hot leg, i.e., 0.7874 m in the present FE model), k_w is the thermal conductivity of water (0.6096 W/m-K at 300 ^{o}C [29]), and N_u is the Nusselt number. The Nusselt number is estimated from the Dittus-Boelter correlation for turbulent heat transfer:

$$N_u = 0.023 Re^{0.8} Pr^n \tag{4.2}$$

where Re is the Reynolds number (assumed 500,000 based on Ref. [30]), and Pr is the Prandtl number (0.8601 at 300 ^{o}C and 15 MPa [29]). Also, the coefficient n in Eq. 4.2 is set equal to 0.3, assuming the fluid is being cooled. With these values, the first approximation of the heat transfer coefficient was calculated to be 616.76 W/m^2-K. Based on this first approximation, multiple heat transfer coefficients were selected, and associated heat transfer analyses were performed to find the approximate coefficient for which the FE simulated temperature at the ID surface reached the desired boundary value at the highest test temperature. From this iterative procedure, we estimated the desired approximate heat transfer coefficient to be 18502.8 W/m^2-K, which is 30 times the first approximation. This heat transfer coefficient was used to determine the maximum ID temperature boundary condition for the HL nozzle. Based on this coefficient and the ID temperature profile of the HL and CL nozzles and RPV, the corresponding temperature-dependent film coefficients were estimated and used in the FE analysis. The OD surfaces of the HL and CL nozzles and RPV were assumed to be at ambient condition or perfectly insulated. In an actual reactor, the OD surface is insulated. However, in the present work, in addition to the insulated OD surface we also performed heat transfer analysis for an ambient OD surface to check how the ambient condition affects the thermal profile across the HL and CL nozzles and RPV. For the ambient condition the temperature was assumed to be approximately 41.5 ^{o}C, which is similar to the containment inside temperature. For example, according to the Westinghouse NPP manual [31], the containment air cooler system is designed to maintain the containment air temperature at or below 120 ^{o}F (or 48.9 ^{o}C). The convective film coefficient for the ambient condition was assumed to be 100 W/m^2-K [32]. Time-dependent heat transfer analysis also requires determination of additional thermal material properties, such as mean coefficient of thermal expansion, thermal conductivity, diffusivity, and specific heat capacity. For the FE model, we used SA-508 carbon steel (or 508 low alloy steel) thermal properties and the corresponding SI unit based properties from our earlier work [11, 12]. The original British unit based data were taken from EPRI report [33] and ASME code [35].

4.2 Thermal Analysis Results

Thermal analysis for the RPV with HL and CL nozzles was performed with the ID temperature boundary condition shown in Figure 3.7 and with the OD surface being either subjected to ambient or insulated conditions. We performed multiple FE simulations using different convective heat transfer or film conditions. The FE simulations were performed in multiple FE steps (total 298), using automated time increments under each step. This multi-step model ensured estimation of a temperature profile at the peak temperature boundary condition without consuming much computational time, in contrast to a single-step based model with smaller fixed time increments. Below shows the heat transfer analysis results obtained for three film conditions.

4.2.1 OD surface ambient condition with ID surface maximum film coefficient of 616.76 W/m^2-K

For the above condition, the estimated temperature histories across the CL, HL, and RPV thickness are shown in Figures 4.1, 4.2, and 4.3, respectively. The spatial distributions of the OD and ID temperature at a typical time (approximately at 391.09 days) are shown in Figure 4.4. Figure 4.2 indicates that the maximum temperature in the ID surface of the HL is approximately 290 ^{o}C, which is well below the required maximum boundary condition temperature of approximately 324 ^{o}C (refer to Figure 3.7).

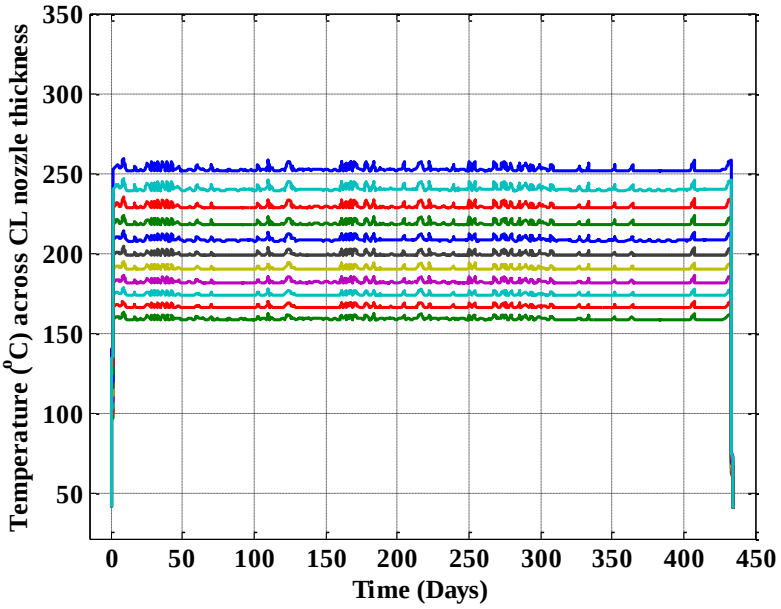

Figure 4.1 Temperature across CL nozzle thickness for OD surface ambient condition with ID surface maximum film coefficient of 616.76 W/m^2-K.

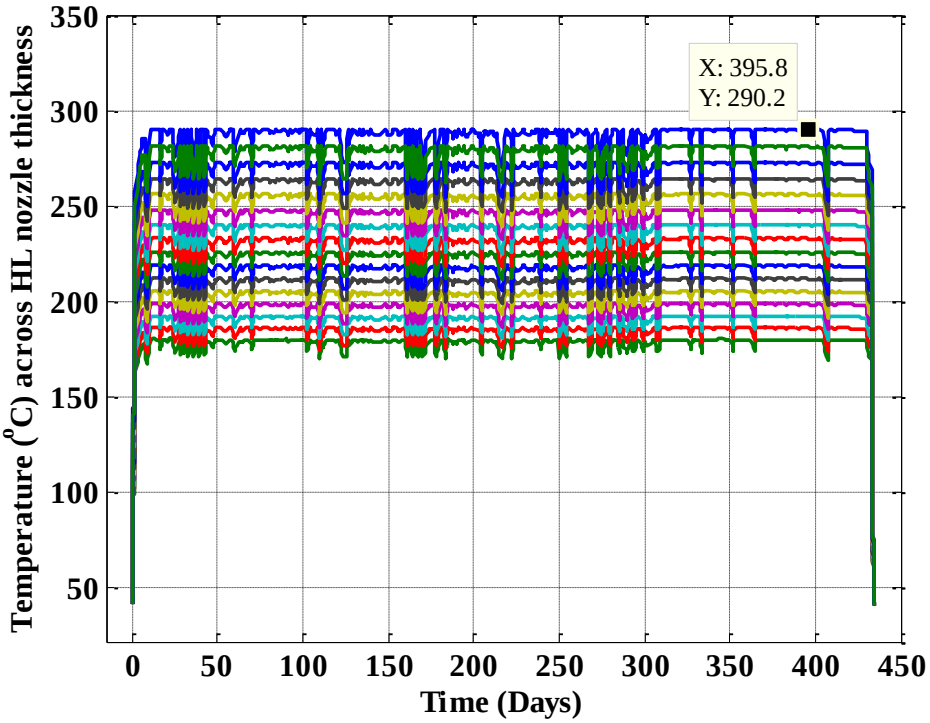

Figure 4.2 Temperature across HL nozzle thickness for OD surface ambient condition with ID surface maximum film coefficient of 616.76 W/m²-K.

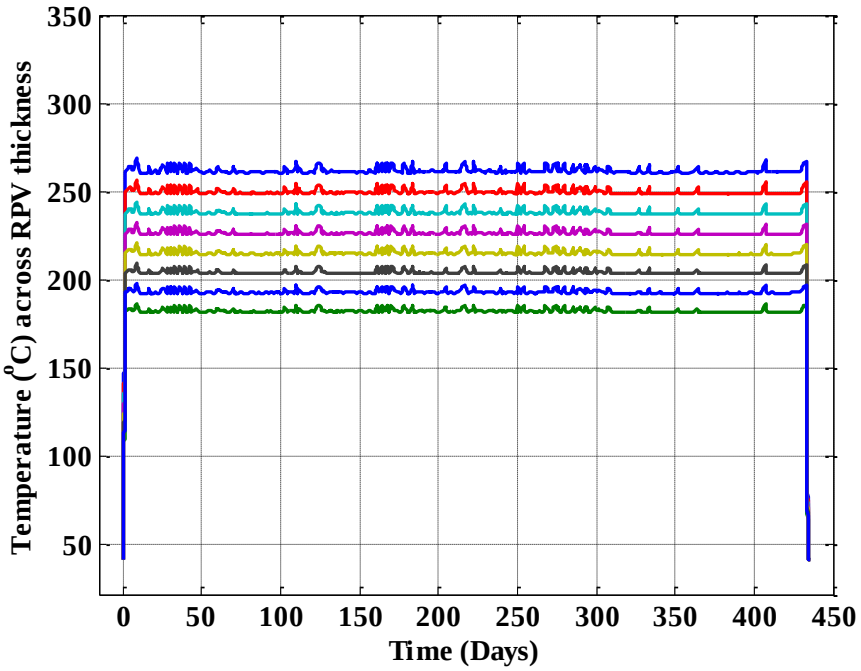

Figure 4.3 Temperature across RPV thickness for OD surface ambient condition with ID surface maximum film coefficient of 616.76 W/m²-K.

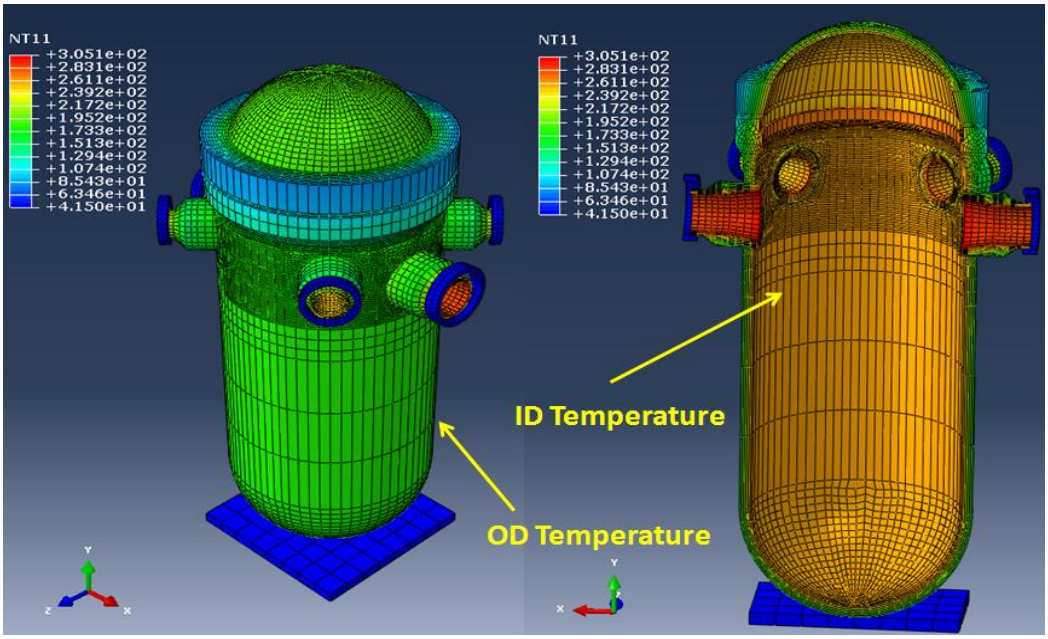

Figure 4.4 The OD and ID temperature spatial distribution at approximately 391.09 days obtained through FE model for OD surface ambient condition with ID surface maximum film coefficient of 616.76 W/m²-K.

4.2.2 OD surface ambient condition with ID surface maximum film coefficient of 18502.8 W/m^2-K

To overcome the shortcomings in using film coefficient of 616.76 W/m^2-K, we performed multiple heat transfer analysis using different film coefficients. From the iterative approach, we found that a film coefficient value of 18502.8 W/m^2-K produces a reasonably accurate ID boundary condition temperature. Under the above condition, the estimated temperature histories across the CL, HL, and RPV thickness are shown in Figures 4.5, 4.6, and 4.7, respectively. The spatial distributions of the OD and ID temperature at a typical time (approximately at 391.09 days) are shown in Figure 4.8. Figure 4.6 indicates that the maximum temperature in the ID surface of the HL is approximately 322.4 ^{o}C, which is comparable to the required maximum boundary condition (ID surface of the HL) temperature of approximately 324 ^{o}C (refer to Figure 3.7).

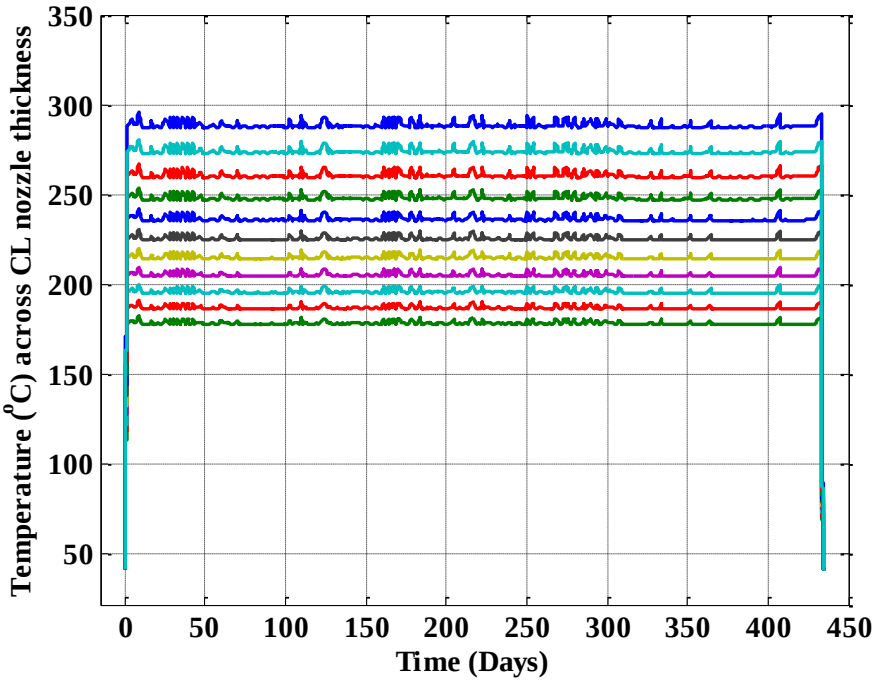

Figure 4.5 Temperature across CL nozzle thickness for OD surface ambient condition with ID surface maximum film coefficient of 18502.8 W/m²-K

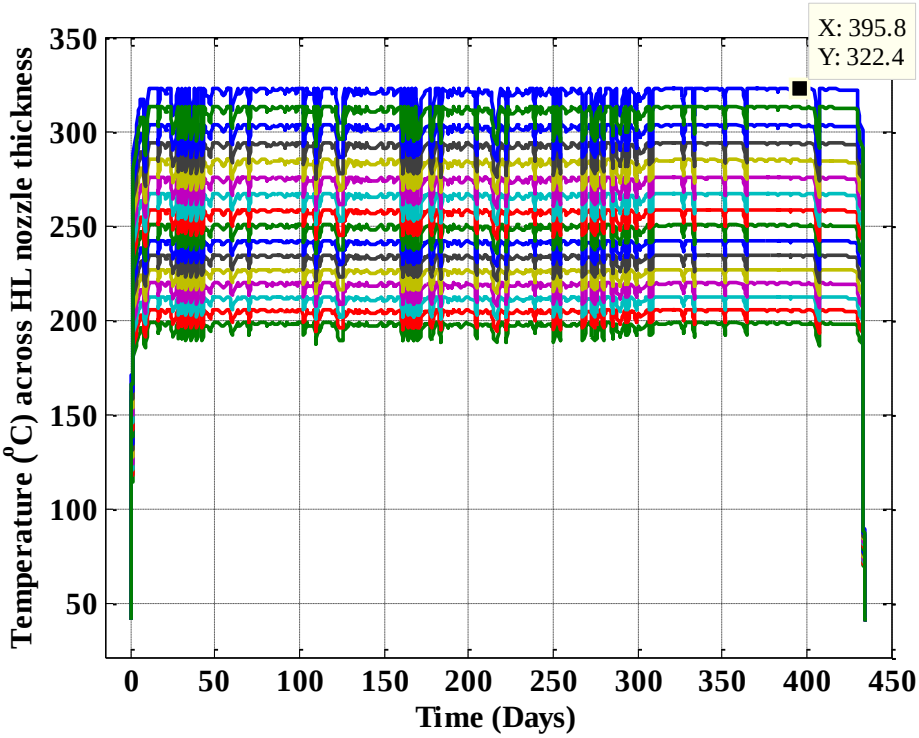

Figure 4.6 Temperature across HL nozzle thickness for OD surface ambient condition with ID surface maximum film coefficient of 18502.8 W/m²-K

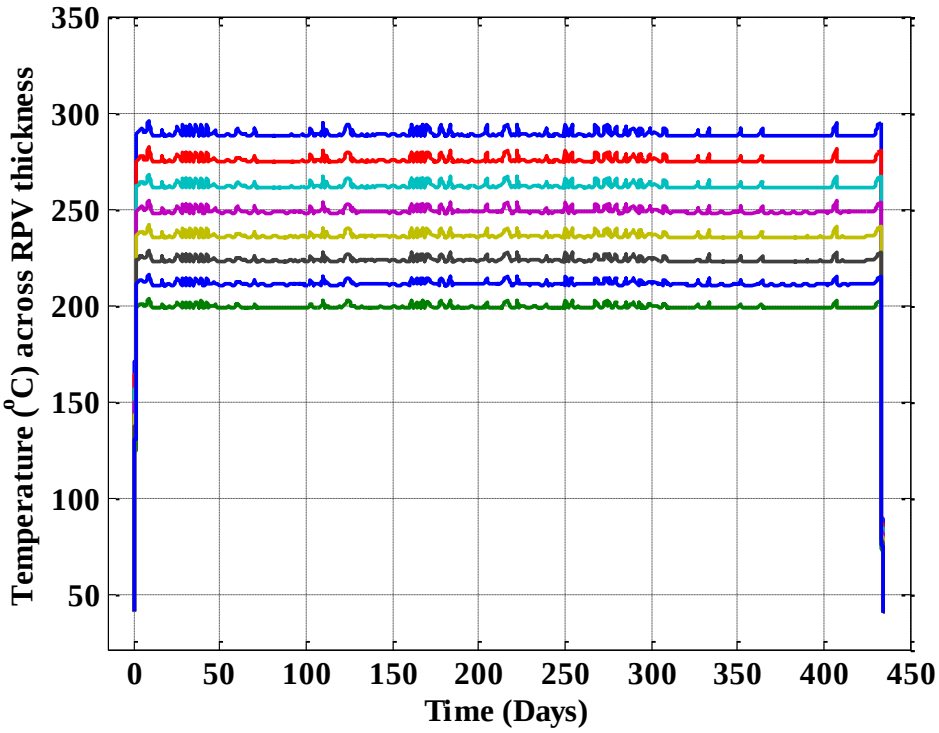

Figure 4.7 Temperature across RPV thickness for OD surface ambient condition with ID surface maximum film coefficient of 18502.8 W/m²-K

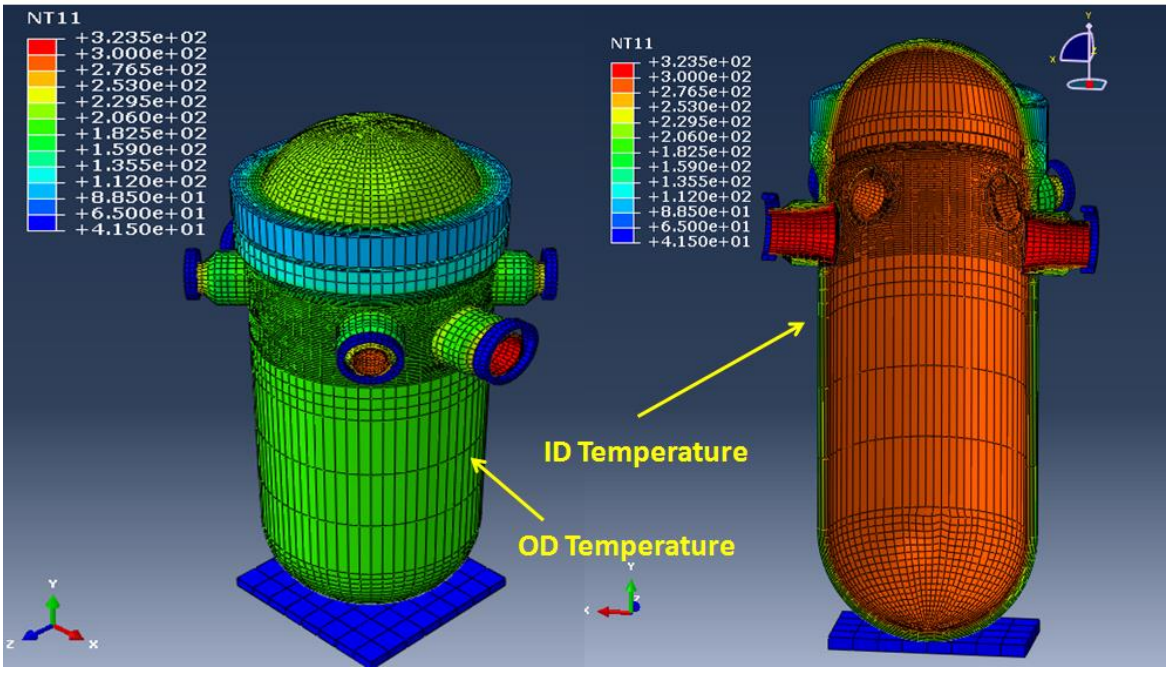

Figure 4.8 Spatial distribution of OD and ID temperature at approximately 391.09 days obtained through FE model for OD surface ambient condition with ID surface maximum film coefficient of 18502.8 W/m²-K

4.2.3 OD surface insulated condition with ID surface maximum film coefficient of 18502.8 W/m^2-K

In addition to the ambient OD surface-temperature boundary condition, we performed a heat transfer analysis assuming that all the OD surfaces of the RPV and nozzles are perfectly insulated. For this condition, we assumed the coolant water film coefficient to be the same as the previous case, i.e., 18502.8 W/m^2-K. Under the above condition, the estimated temperature histories across the CL, HL, and RPV thickness are shown in Figures 4.9, 4.10, and 4.11, respectively. The spatial distributions of the OD and ID temperature at a typical time (approximately at 391.09 days) are shown in Figure 4.12. Figure 4.10 indicates that the maximum temperature in the OD surface of the HL is approximately 323.8 ^{o}C, which is approximately the same as the required maximum boundary condition temperature of approximately 324 ^{o}C (refer to Figure 3.7). However, compared to the previous two cases, the variation of temperature with thickness for the insulated condition is not significant (Figure 4.13). That finding means that at a given time the thickness of the RPV and HL/CL nozzle component mostly stays under the isothermal condition. The difference in variation of temperature with thickness for the case discussed in Section 4.2.2 can clearly be seen from Figure 4.13. Note that a large temperature variation across the thickness may create larger thermal-mechanical stress. A more accurate simulation of the reactor thermal profile requires modeling the reactor insulation and the gap between the insulation and OD surfaces. However, for further FE analysis, such as the thermal-mechanical stress analysis discussed in later sections, for simplicity, we used the nodal temperature distributions obtained under the ideal/perfectly insulated condition.

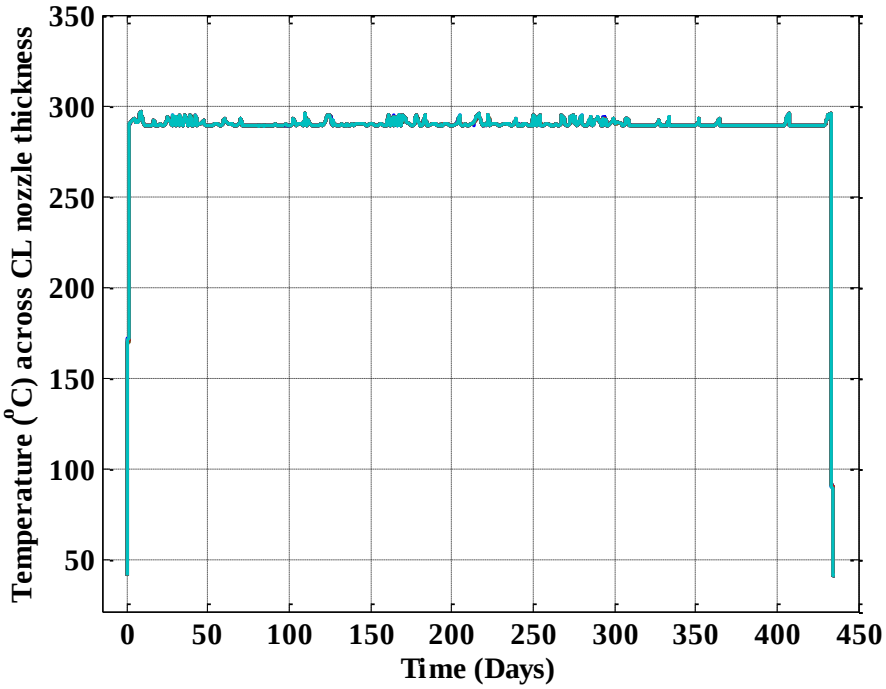

Figure 4.9 Temperature across CL nozzle thickness for OD surface insulated condition with ID surface maximum film coefficient of 18502.8 W/m^2-K.

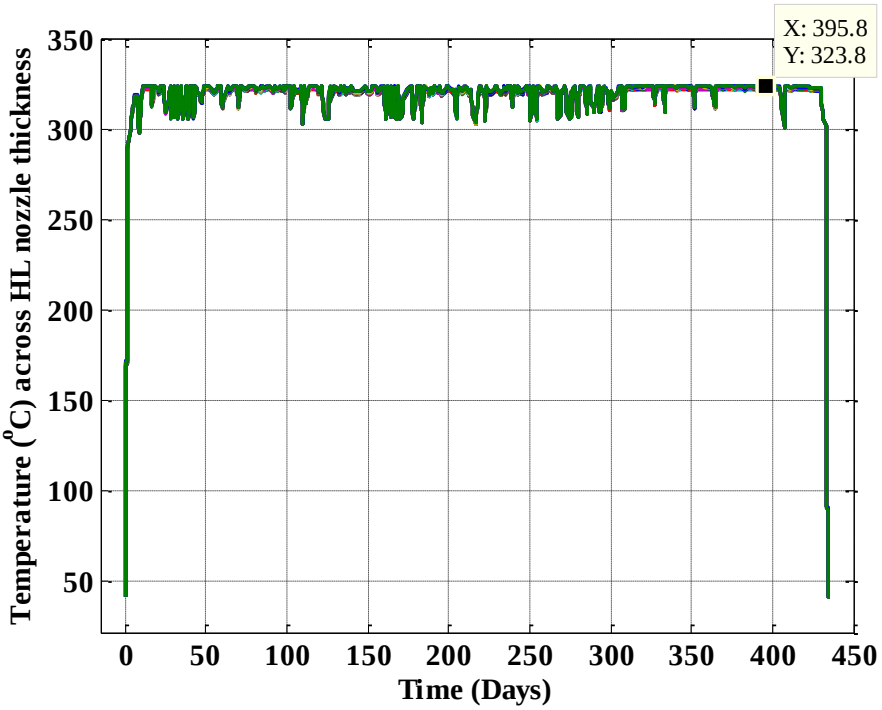

Figure 4.10 Temperature across HL nozzle thickness for OD surface insulated condition with ID surface maximum film coefficient of 18502.8 W/m²-K.

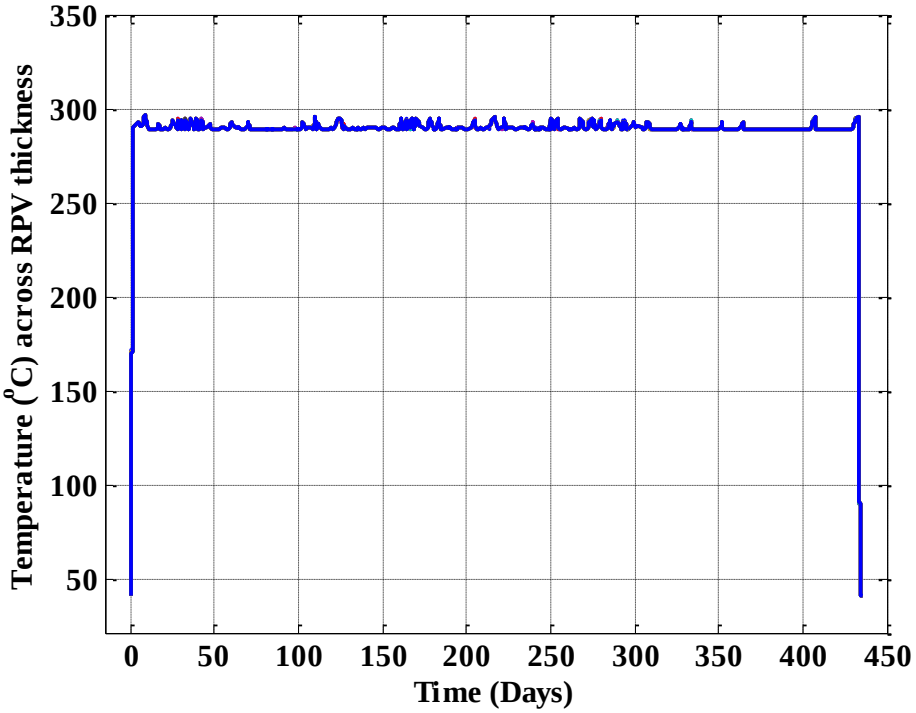

Figure 4.11 Temperature across RPV thickness for OD surface insulated condition with ID surface maximum film coefficient of 18502.8 W/m²-K

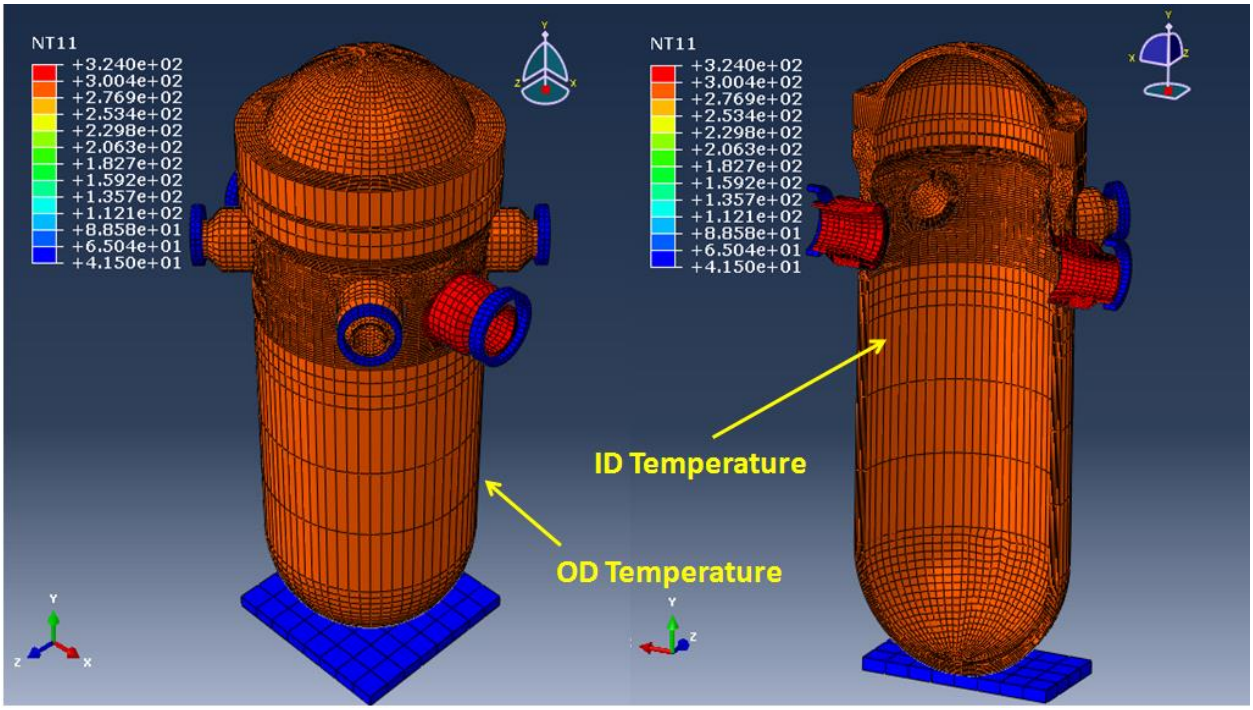

Figure 4. 12 Spatial distribution of OD and ID temperature at approximately 391.09 days obtained through FE model for OD surface insulated condition with ID surface maximum film coefficient of 18502.8 W/m²-K.

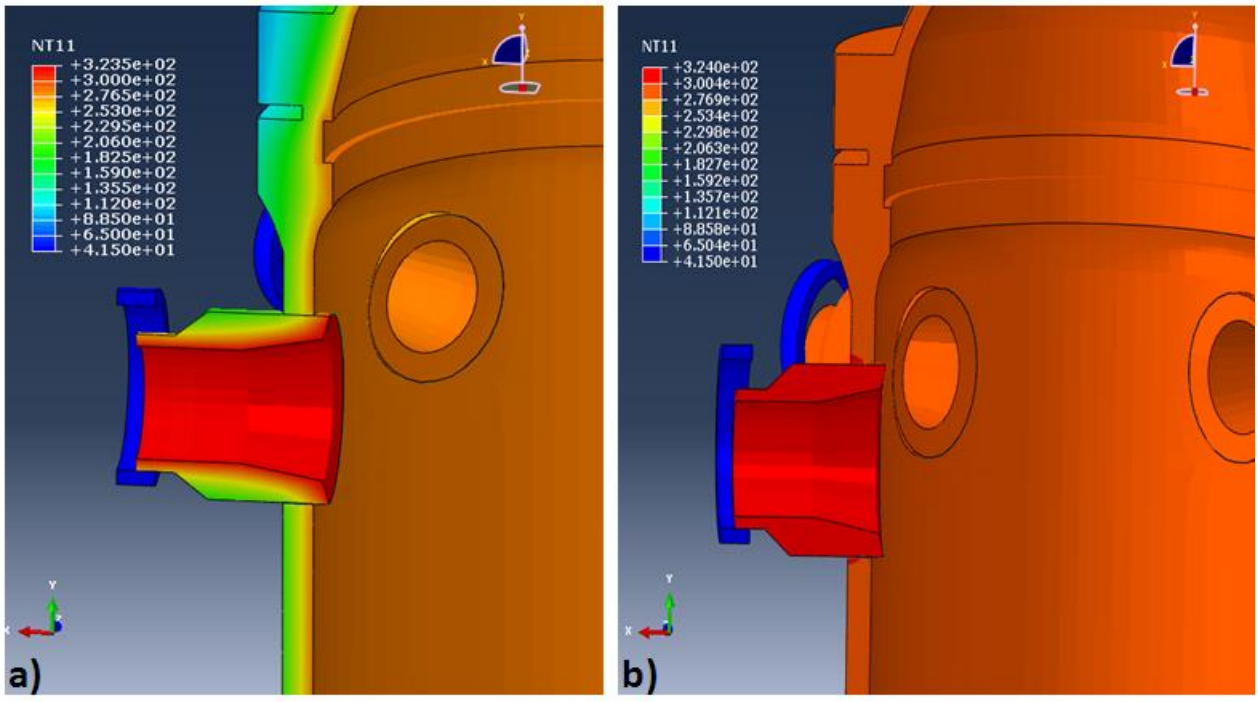

Figure 4.13 Thickness variation of temperature for case discussed in a) Section 4.2.2 and b) Section 4.2.3.

5 Material Properties for Structural Analysis

In our earlier work [18] we estimated the elastic-plastic material property of the 508 LAS specimen under tensile and fatigue loading (either under in-air or PWR water conditions). Some of the reported material properties are used in this work. In the discussed stress analysis work, we used material parameters from tensile test ET-T08 (300 ^{o}C, in-air condition) and fatigue test RT-F08 (22 ^{o}C, in-air condition), ET-F24 (300 ^{o}C, in-air condition), and EN-F20 (300 ^{o}C, PWR condition). For easier reference, some of the important material properties are reproduced below. The details of the material testing and property estimation procedures can be found in reference [18].

Figure 5.1 shows the cycle-dependent elastic modulus estimated under different conditions. Figures 5.2, 5.3, and 5.4 show the cycle/time-dependent 0.05% offset yield stress, kinematic hardening parameter C_1, and kinematic hardening parameter γ_1, respectively. In the discussed work we used materials properties based on the 0.05% offset yield stress. Note that, from the fatigue test data, we only used the material properties associated with the half-life of the corresponding fatigue test.

Table 5.1 summarizes the material properties used for the elastic-plastic stress analysis. In general, for elastic-plastic stress analysis, commercially available software such as ABAQUS requires elastic modulus (E), Poisson's ratio, yield stress (σ_{YL}), and kinematic hardening parameters (C_1 and γ_1) as input parameters. These parameters at temperatures of 22 ^{o}C and 300 ^{o}C (as given in Table 5.1) were provided as input to ABAQUS. For temperatures between 22 ^{o}C and 300 ^{o}C and beyond 300 ^{o}C (note the maximum temperature in the discussed work is 324 ^{o}C), the material properties were linearly interpolated/extrapolated. For all temperatures, Poisson's ratio was assumed constant and equal to 0.3. In addition to the required material properties for elastic-plastic stress analysis, we need to provide additional material properties for performing crack initiation/propagation analysis with the extended finite element method (XFEM). We performed stress analysis of the RPV with/without preexisting cracks. To perform the stress analysis of a component with crack initiation/propagation modeling, ABAQUS requires damage initiation and propagation criteria depending on the chosen failure theory. In the discussed work we used criteria based on the maximum principal stress for crack initiation from a notch (in the present case, a preexisting crack). The crack initiation criteria are obtained from the following equation:

$$f = \frac{\left\langle \sigma^{p}_{\max} \right\rangle}{\sigma^{p}_{cr}} = \begin{cases} \geq 1 + f_{tol} & \textit{crack will initiate} \\ < 1 + f_{tol} & \textit{crack will not initiate} \end{cases} \tag{5.1}$$

where $\sigma^{p}_{\max}$ is the solution-dependent maximum principal stress, and σ^{p}_{cr} is the critical principal stress that has to be provided as input. In Eq. (5.1), the symbol $\langle\ \rangle$ represents Macaulay brackets with $\left\langle \sigma^{p}_{\max} \right\rangle = 0$ if $\sigma^{p}_{\max} < 0$, i.e., when the maximum principal stress is purely compressive. In our work we chose the critical principal stress as

$$\sigma^{p}_{cr} = \frac{\sigma_{YL} + \sigma_{u}}{2} \tag{5.2}$$

where σ_{YL} and σ_u are the yield stress and ultimate stress corresponding to any particular temperature, respectively. For estimating σ^{p}_{cr} for the discussed stress analysis cases, we chose parameters from corresponding tensile tests (T06 and T08). The selected critical principal stress (refer to Eq. 5.2) is based on our earlier work [35], for which the FE model estimated data fairly matched with corresponding

experimental data. Similar σ_{YL} and σ_u dependent values of σ_{cr}^{p} were also used by another research group [35], which had verified their XFEM-based results with corresponding experiment data.

In addition to the critical principal stress, ABAQUS requires damage propagation criteria for damage evolution within an element. We used a linear energy-based criteria for which ABAQUS requires critical fracture energy. We estimated the critical fracture energy using the fracture toughness data (for 533 grade low alloy steel) given in reference [37] and elastic modulus data given in Table 5.1, based on linearly interpolated ANL tensile test data. The critical fracture energy G_{IC} can be estimated using the following relation:

$$G_{IC} = \frac{K_{IC}^2}{E} \tag{5.3}$$

where K_{IC} is the fracture toughness. The temperature-dependent fracture toughness data (for 533 grade low alloy steel) are shown in Figure 5.5. The corresponding estimated critical fracture energy data are shown in Figure 5.6.

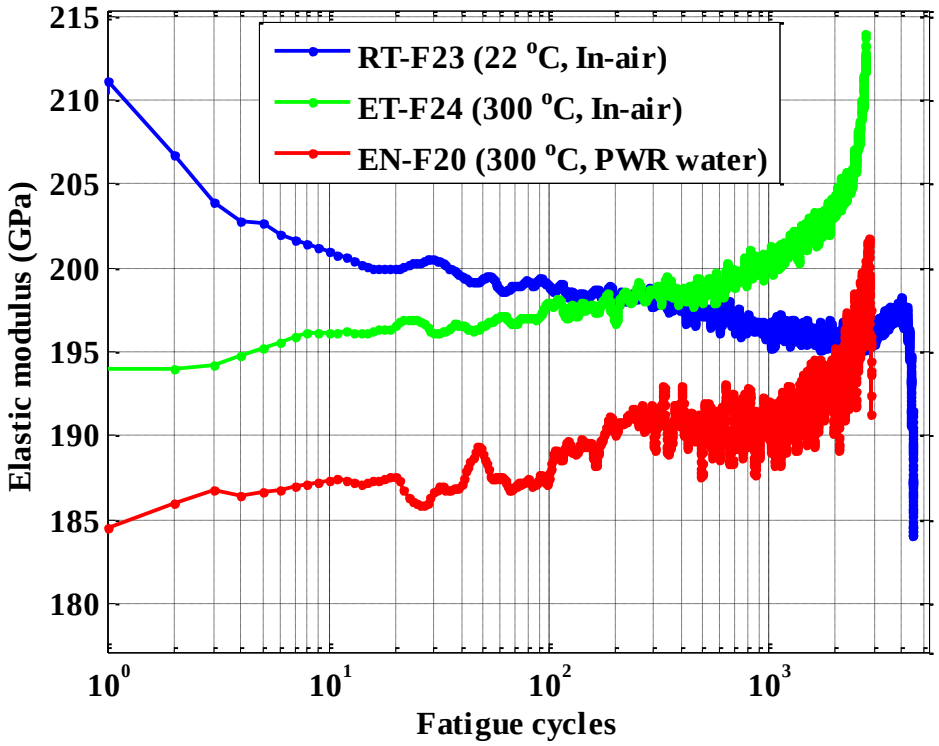

Figure 5.1 Elastic modulus for 508 LAS base metal specimens fatigue tested under different conditions [18].

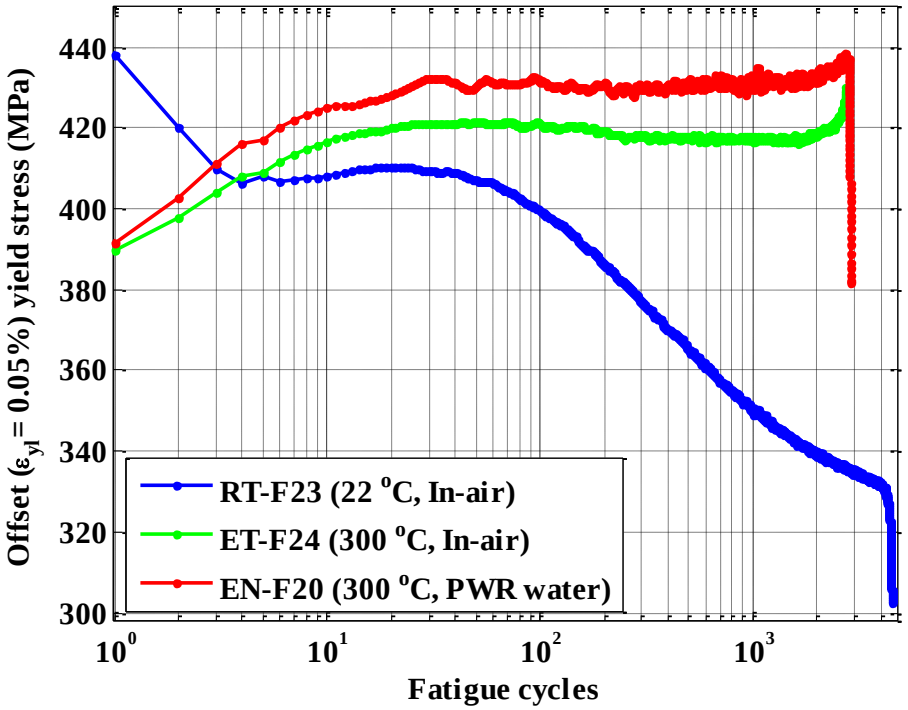

Figure 5.2 Offset-strain (0.05%) yield limit stress for 508 LAS base metal specimens fatigue tested under different conditions [18].

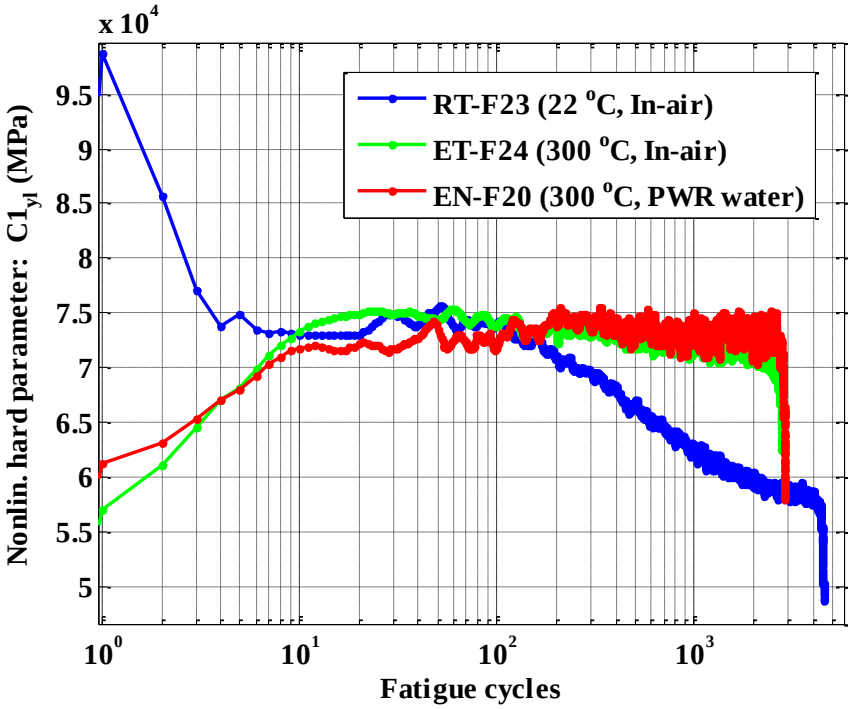

Figure 5.3 Nonlinear kinematic hardening parameter C_1 (0.05% offset strain stress used as yield stress) for 508 LAS base metal specimens fatigue tested under different conditions [18].

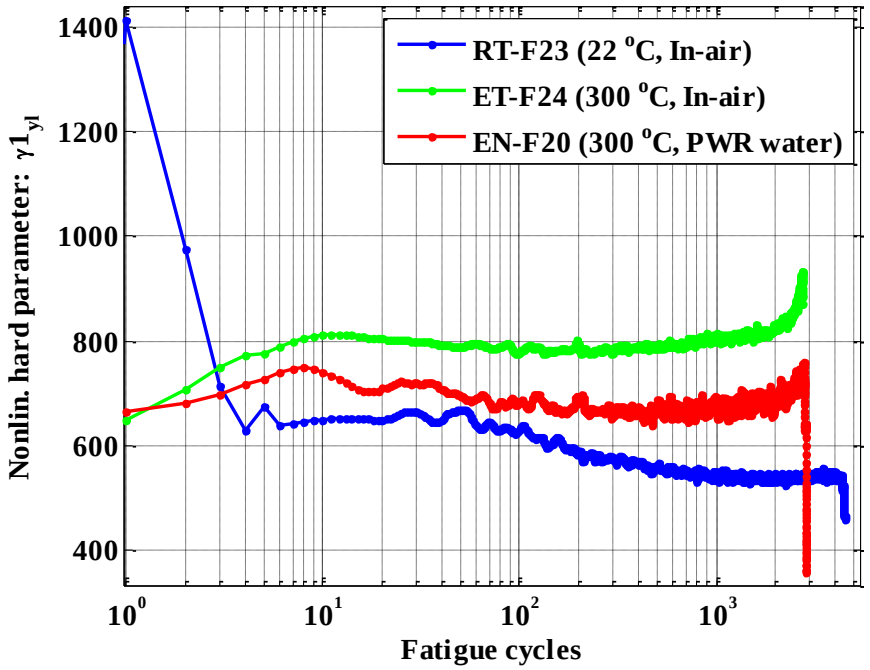

Figure 5.4 Nonlinear kinematic hardening parameter γ_1 (0.05% offset strain stress used as yield stress) for 508 LAS base metal specimens fatigue tested under different conditions [18].

Table 5. 1 Material model parameters (0.05% offset strain stress used as yield limit stress) for 508 LAS base metal specimens at selected fatigue cycles and for tensile tests [18].

Tensile test or fatigue test cycle no.		**Env. type**	**E (GPa)**	σ_{YL} **(MPa)**	σ_u **(MPa)**	σ_{cr}^{p} **(MPa)**	**Nonlin. Model** C_1 **(MPa)**	**Nonlin. Model** γ_1 **(MPa)**
Tensile tests (T06, and T08 data)		RT	209.19	427.31	563.18	495.25	2150.4	-13.087
		ET	197.57	415.15	610.28	512.71	10699	49.624
Selected fatigue cycles (RT-F23, ET-F24, and EN-F20)	Cy=1	EN	184.51	391.55	-	-	61236	666.75
	Cy=N/2 for RT-F23= 2247, ET-F24= 1375, and F20= 1438	RT	196.25	338.37	-	-	59082	537.76
		ET	201.61	416.82	-	-	71618	809.75
		EN	190.18	432.1	-	-	72998	675.49

* RT, ET, and EN symbolize room temperature, elevated temperature, and PWR environment, respectively.

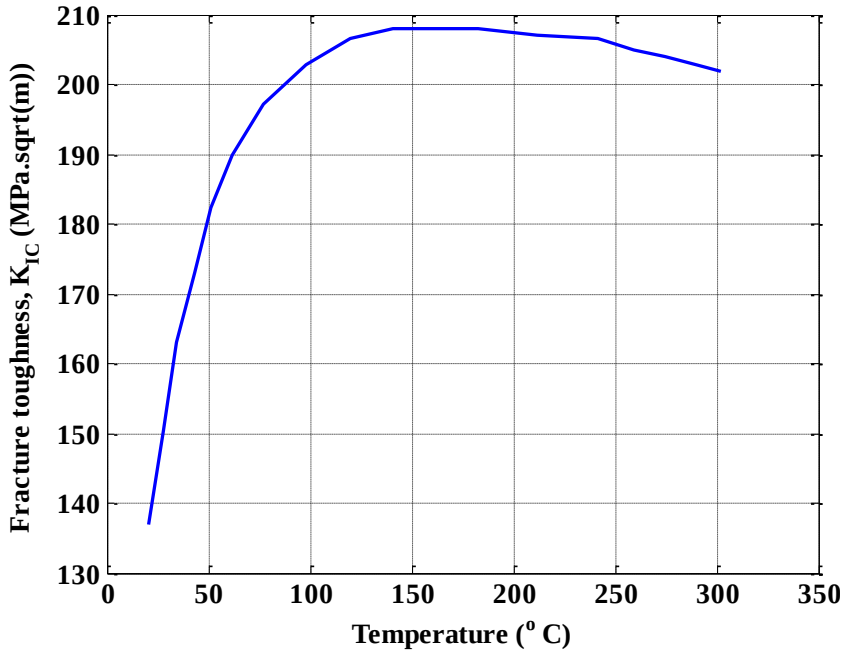

Figure 5.5 Fracture toughness data (for 533 LAS) taken from [35].

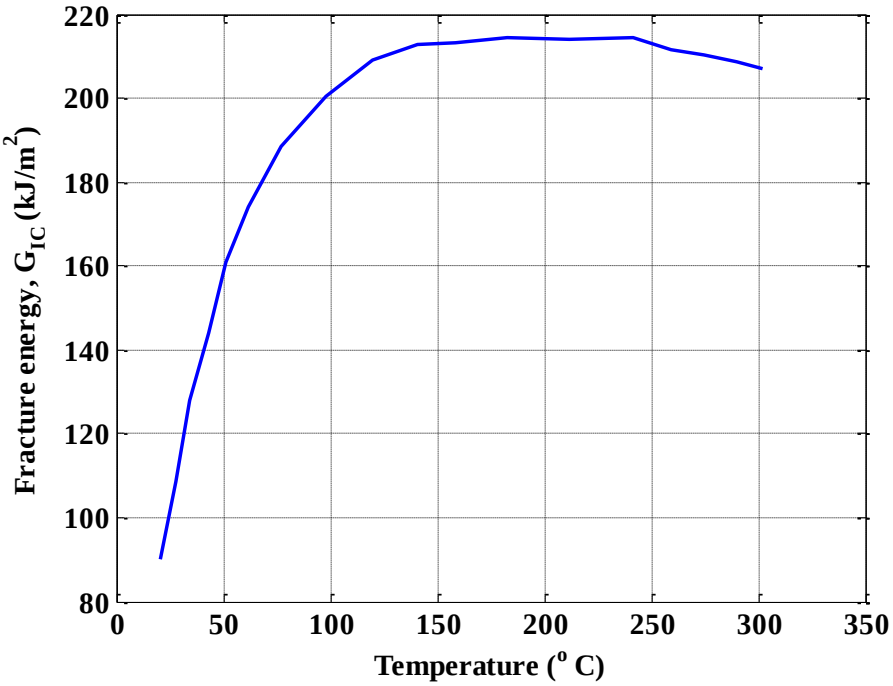

Figure 5.6 Estimated critical fracture energy for 533 LAS and used in the XFEM-based simulation.

6 Stress Analysis of Laboratory Specimens under Isothermal Fatigue Loading

As mentioned in the previous section we used the elastic-plastic material properties estimated through our earlier work [18] for structural analysis of the RPV. However, before performing structural analysis of the RPV, we modeled some of the laboratory specimens, which experiment data were used for estimating the elastic-plastic material properties. This was done to check whether or not the FE models, based on estimated material properties, are able to mimic the experimental results (stress-strain curves). For this purpose, we developed an FE model of a tensile test specimen and a fatigue test specimen. The related results are discussed below.

6.1 FE Model of T08 Tensile Test

The T08 tensile test was conducted using a 508 LAS specimen at a temperature of 300 ^{o}C under in-air condition. The test was conducted by controlling the strain with a strain rate of 0.1%/s. For simplicity we developed an equivalent load-controlled 3-D FE model to estimate the corresponding stress-strain states at a specimen gauge area. For material properties we used the T08 material properties given in Table 5.2. The resulting stress-strain curves (both based on axial stress –S22 and Von-Mises equivalent stress) are shown in Figure 6.1. This figure also shows the corresponding experimental stress-strain curve. A good correlation is evident between the experimentally observed and FE estimated stress-strain curves.

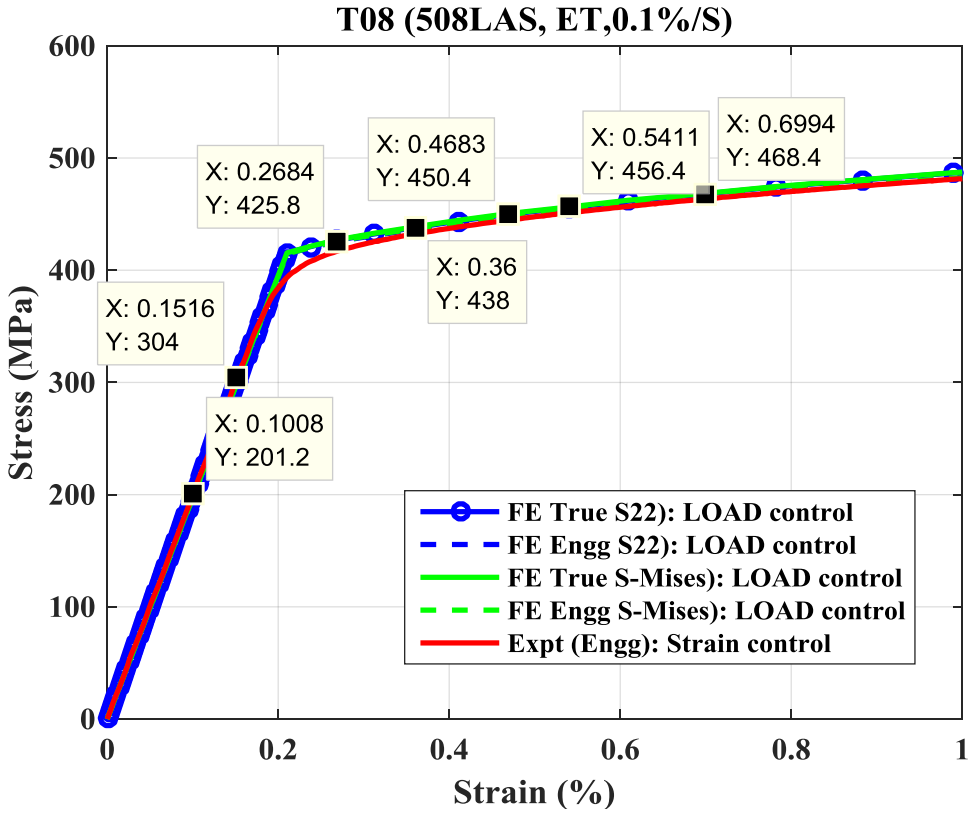

Figure 6.1 Experiment and calculated FE stress-strain curve for T08 tensile test.

6.2 FE Model of EN-F20 Fatigue Test

In addition to the above tensile test FE model, we created an FE model for verification of cyclic- or time-dependent material properties. This model was created to simulate the EN-F20 fatigue specimen, which was made from 508 LAS metal and was tested under PWR primary water condition at a temperature of 300 ºC. The test was conducted by controlling the frame crosshead displacement or stroke. The details of the test process can be found in our earlier work [18, 19].

To simulate the test condition for the first few fatigue cycles, we created a stroke-control FE model using the EN-F20 material properties given in Table 5.1. Since we intended to simulate stress-strain states of the first few fatigue cycles, we used the material properties associated with the first fatigue cycle (that is, the material properties estimated using the stress-strain curve in the first cycle of the EN-F20 test). The FE simulation was conducted using multiple steps with automatic time increment option to avoid a large simulation time and generating a large data file. Multiple step simulation forces ABAQUS to perform calculation at peak loading inputs. Note in a single step model if automated time increment option is chosen, ABAQUS may jump important peak loads. To avoid this it is required to choose fixed increment based option with smaller time increments. However smaller time increments create large data file and requires large simulation time. Figure 6.2 shows experiment versus FE model stroke input for the first few cycles. This figure shows a total of eight FE steps with different time periods and peak amplitudes S1, S2…S8. This multi-step FE procedure forced the ABAQUS software to capture the stress-strain state at least at the peak or at the end increment of individual steps. However, ABAQUS was allowed to choose time increments within a step, depending on the convergence requirement (to satisfy the yield criteria or yield function). Figure 6.3 shows the FE simulated profile for the accumulated plastic strain at peak stroke inputs S1, S2…S8 (refer to Figure 6.2). Figures 6.4 and 6.5 show the experimental and simulated gauge area strain and stress histories. Figures 6.4 and 6.5 indicate that the FE model based on estimated material properties accurately captures the experimental stress-strain state. With this confidence we further used the estimated material properties for thermal-mechanical stress analysis of the RPV. The related model and results are discussed in the next sections.

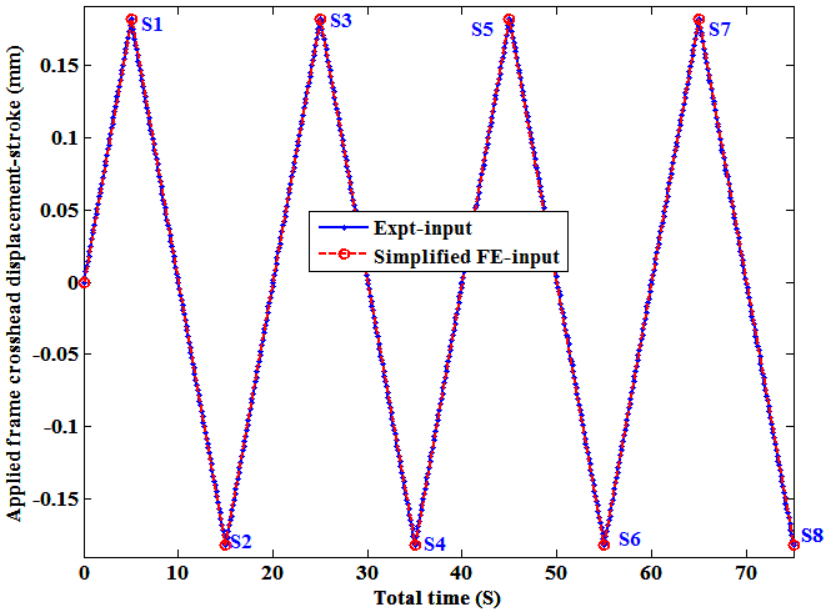

Figure 6.2 Experimental and FE input for EN-F20 fatigue specimen. The FE simulation was conducted over multiple steps (with peak amplitudes S1, S2…S8).

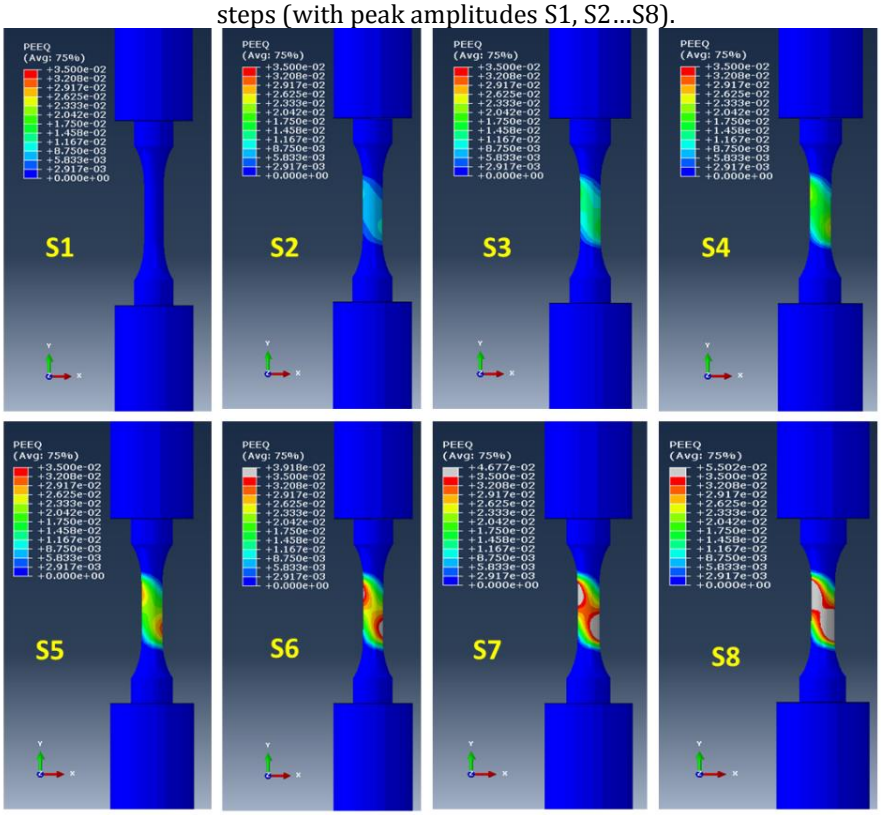

Figure 6.3 FE simulated profile for accumulated plastic strain at peak stroke amplitudes S1, S2…S8 (shown in Figure 6.2).

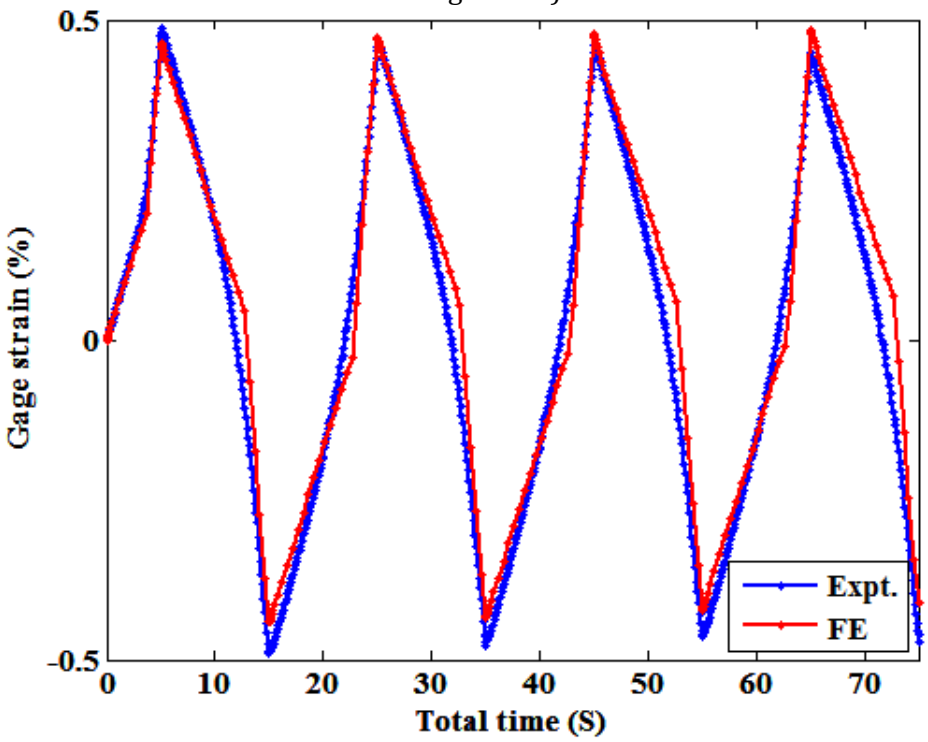

Figure 6.4 Experimental and FE simulated gauge area strain.

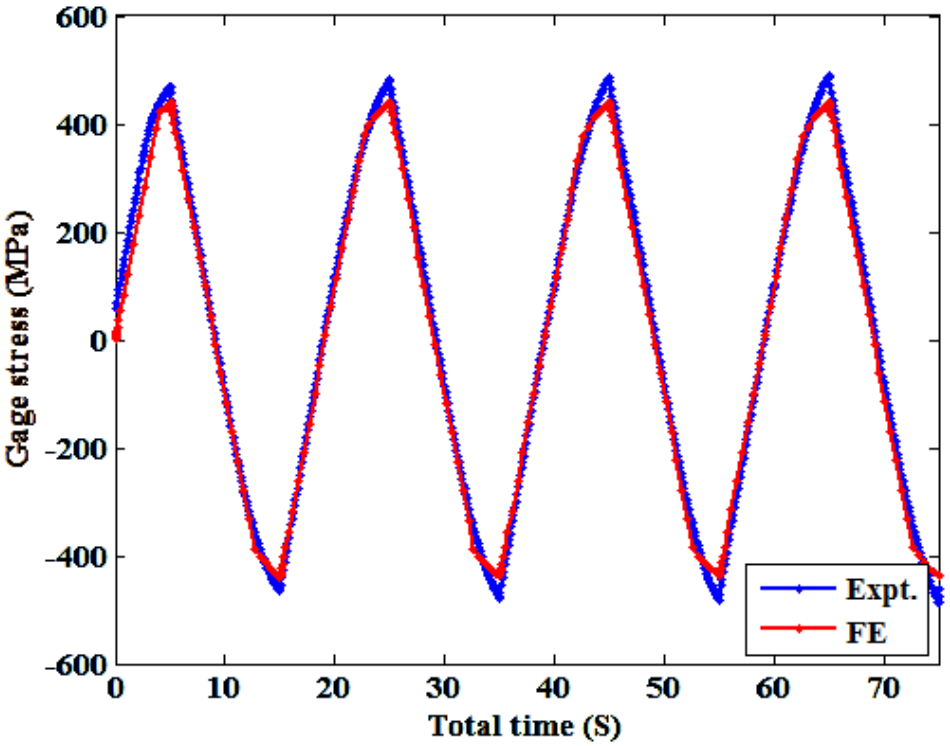

Figure 6.5 Experimental and FE simulated gauge area stress.

7 Thermal-Mechanical Stress Analysis of RPV and Nozzles without Preexisting Cracks

We performed thermal-mechanical stress analysis using the RPV FE model discussed in Section 2. Nodal temperatures from the heat transfer analysis discussed earlier were used as input. We used nodal temperature data from heat transfer results estimated for the insulated OD surface of the RPV (refer to Section 4.2.3). In addition to the nodal temperature input, we modeled the internal coolant water pressure. The time-dependent pressure history shown in Figure 3.8 was used as the ID surface pressure boundary for the RPV, HL, and CL nozzles. For the nozzles we assumed they had no preexisting cracks and had been subjected to the same pressure boundary conditions. Sequentially coupled thermal-mechanical stress analyses were conducted with predetermined temperature data from thermal analysis. Two simulations were performed with different sets of material properties to study the effect of in-air versus PWR conditions. Both simulations were conducted using the half-life (cycle = N/2, where N is the total fatigue life) material properties given in Table 5.1. The two simulation conditions are:

- Case 1 (in-air condition): Elastic-plastic material properties were interpolated/extrapolated using the elastic-plastic material properties estimated from half-life (cycle=N/2) stress-strain data of RT-F23 (in-air, 22^{o}C) and ET-F24 (in-air, 300 ^{o}C) tests.
- Case 2 (PWR water condition): Elastic-plastic material properties were interpolated/extrapolated using the elastic-plastic material properties estimated from half-life (cycle=N/2) stress-strain data of RT-F23 (in-air, 22^{o}C) and EN-F20 (PWR water, 300 ^{o}C) tests. We assumed at room temperature there is no environmental effect on material properties.

Figures 7.1, 7.3, and 7.5 show a comparison between case 1 and case 2 of thermal strain at maximum stressed locations or at corresponding finite elements (refer to Figure 7.21) for the CL nozzle, HL nozzle, and RPV shell, respectively. Figures 7.2, 7.4, and 7.6 show the magnified version of Figures 7.1, 7.3, and 7.5, respectively. Figures 7.7 and 7.8 show the gauge area temperature and thermal strain observed during the heat-up procedure (approximately first 5.5 hours) of a typical 508 LAS specimen tensile tested at ANL [18]. Note that, before conducting an isothermal tensile/fatigue test we heat up the specimen in a series of steps similar to those in an actual reactor. During the heat-up procedure we maintain a load-controlled condition with approximately zero load as set point and allow the specimen to thermally expand. This creates nearly zero stress condition but with growing thermal strain in the specimen. For the mentioned example we heated up the 508 LAS specimen from room temperature to 300 ^{o}C over approximately 5.5 hours. During heat-up we measured the gauge area thermal strain. Comparing Figures 7.1 (CL nozzle thermal strain) and 7.5 (RPV shell thermal strain) with Figure 7.8 indicates that the FE-estimated thermal strain histories during the initial heat-up procedure correlate with the experimentally observed thermal strain. Note that the RPV and CL nozzle ID surfaces were subjected to a temperature boundary condition with maximum temperature of approximately 290 ^{o}C. In addition to thermal strain, we estimated the histories of total strain and Von-Mises stress at the above-mentioned maximum stress locations. Figures 7.9, 7.11, and 7.13 show the total strain histories for the CL nozzle, HL nozzle, and RPV shell, respectively, obtained from the case-1 and case-2 FE models. Figures 7.10, 7.12, and 7.14 show the magnified version of Figures 7.9, 7.11, and 7.13, respectively.

Figures 7.15, 7.17, and 7.19 show the corresponding comparison of the Von-Mises stress for the CL nozzle, HL nozzle, and RPV shell, respectively. Figures 7.16, 7.18, and 7.20 show the magnified version of Figures 7.15, 7.17, and 7.19. Furthermore, Figure 7.21 shows the example temperature versus Von-Mises stress profile near the nozzle area (at different instances during heat-up and full power) obtained through the case-1 FE simulation (in-air condition).

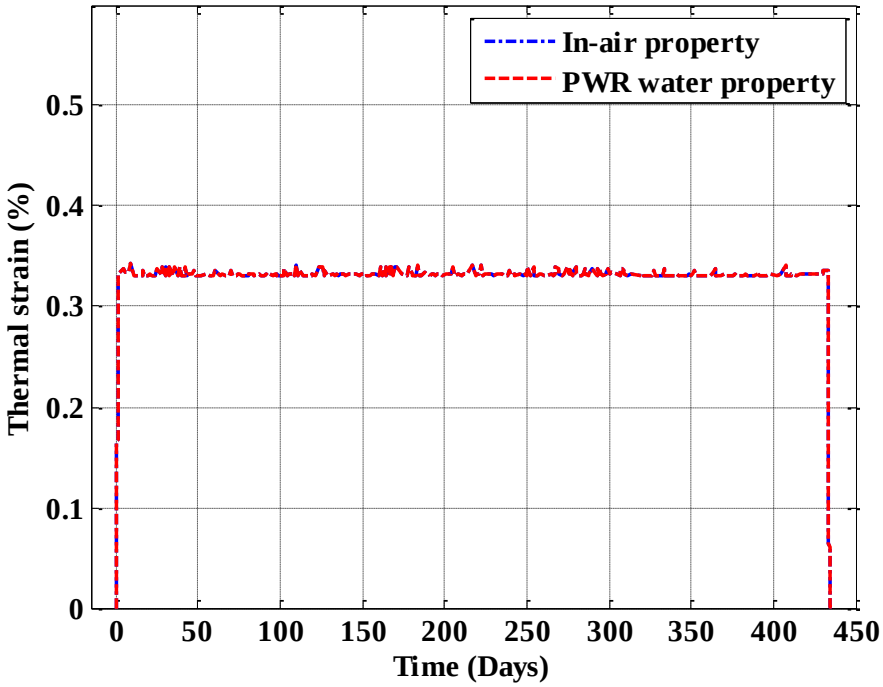

Figure 7. 1 Thermal strain histories estimated at a typical stressed element of CL nozzle for in-air and PWR water conditions.

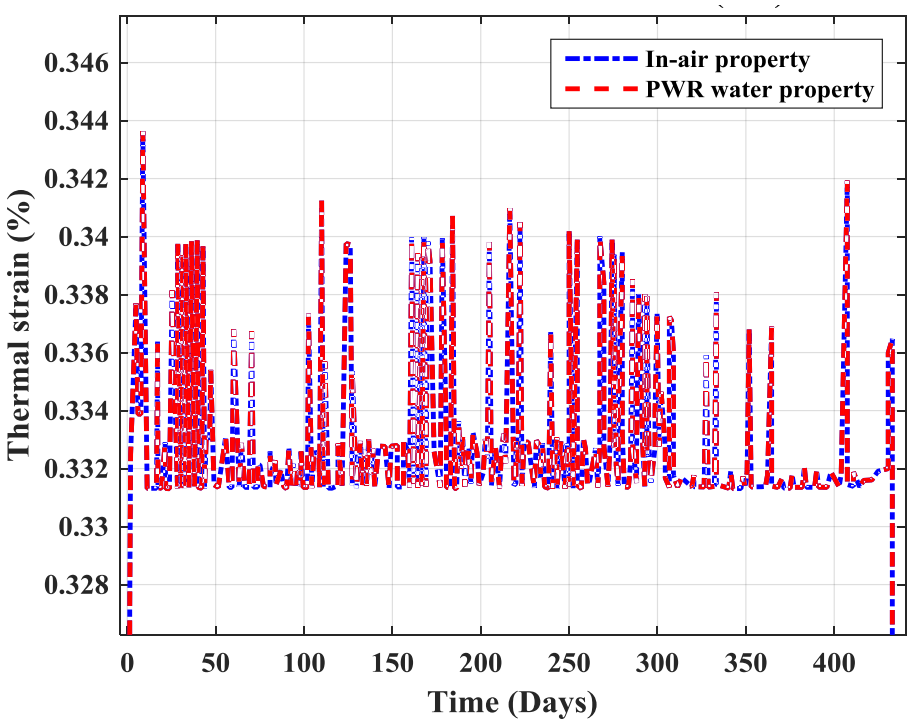

Figure 7. 2 Magnified form of Figure 7.1.

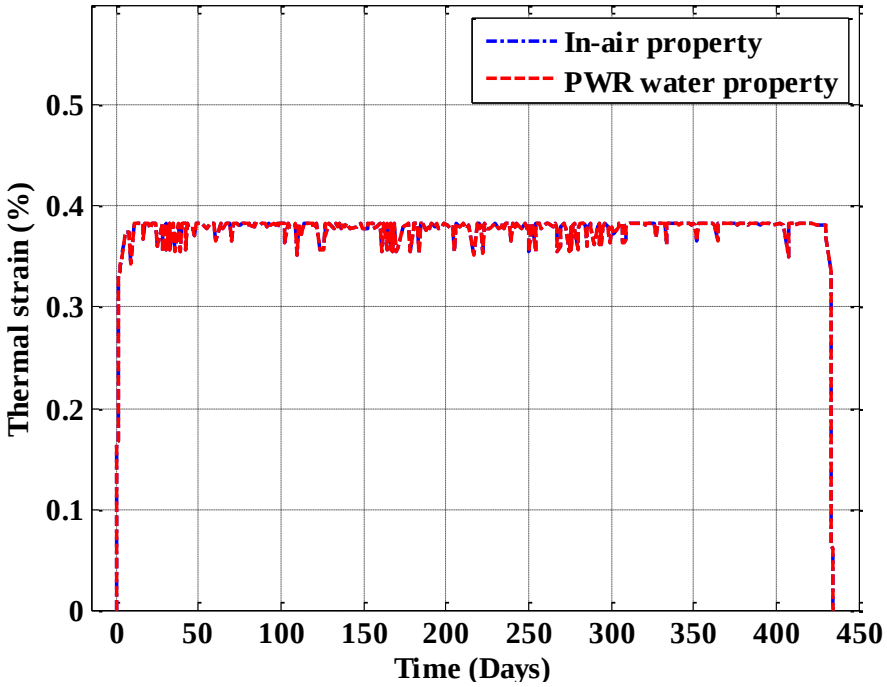

Figure 7. 3 Thermal strain histories estimated at a typical stressed element of HL nozzle for in-air and PWR water conditions.

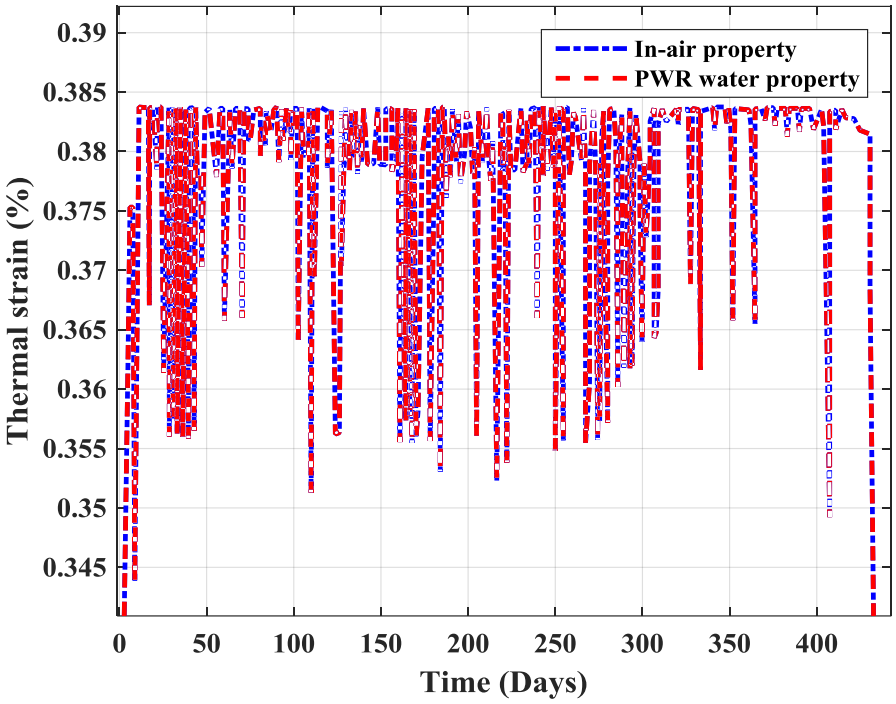

Figure 7. 4 Magnified form of Figure 7.3.

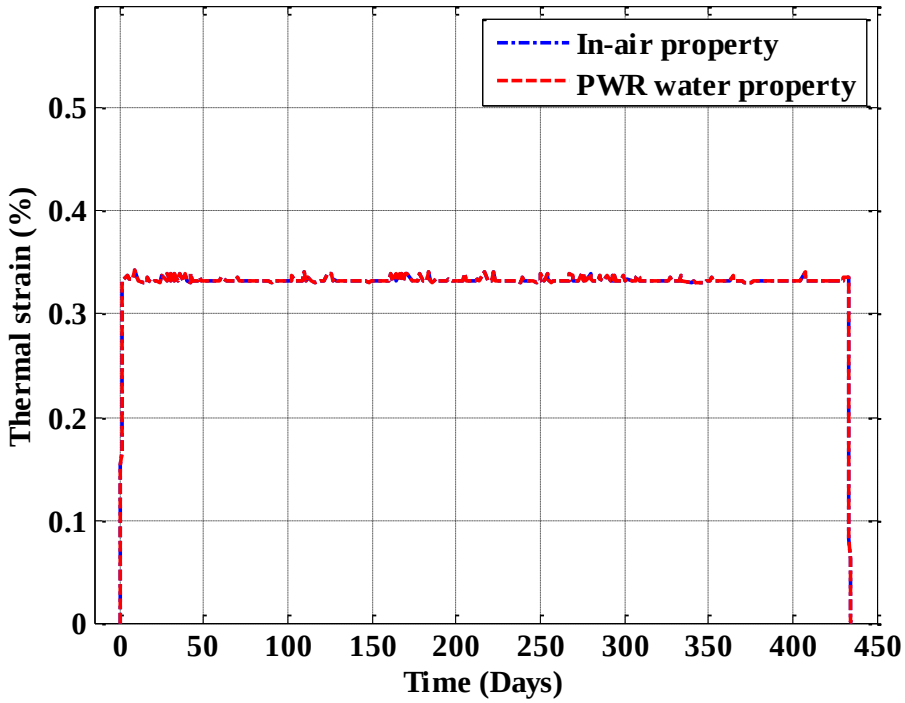

Figure 7. 5 Thermal strain histories estimated at a typical stressed element of RPV shell for in-air and PWR water conditions.

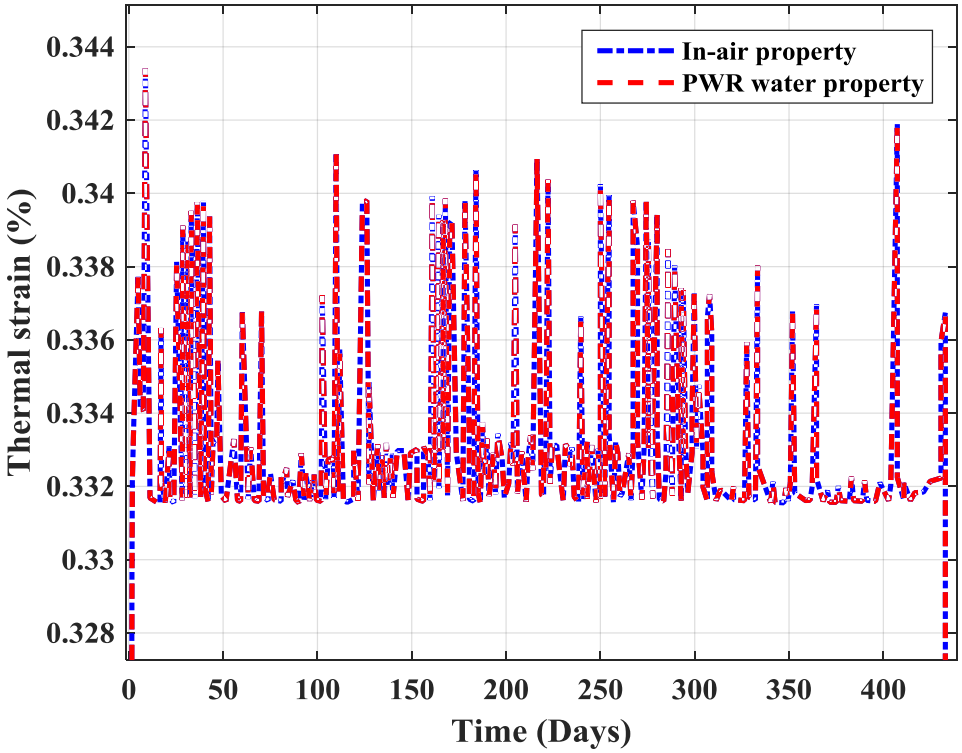

Figure 7. 6 Magnified form of Figure 7.5.

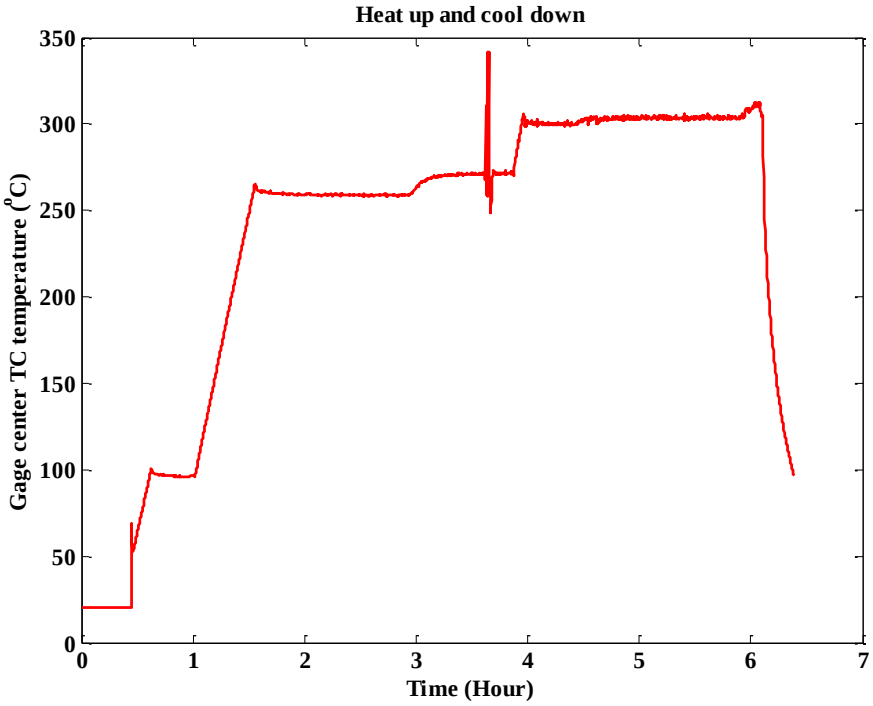

Figure 7. 7 Temperature measured at gauge center thermocouple of a typical 508 LAS specimen tensile test (conducted at ANL [18]).

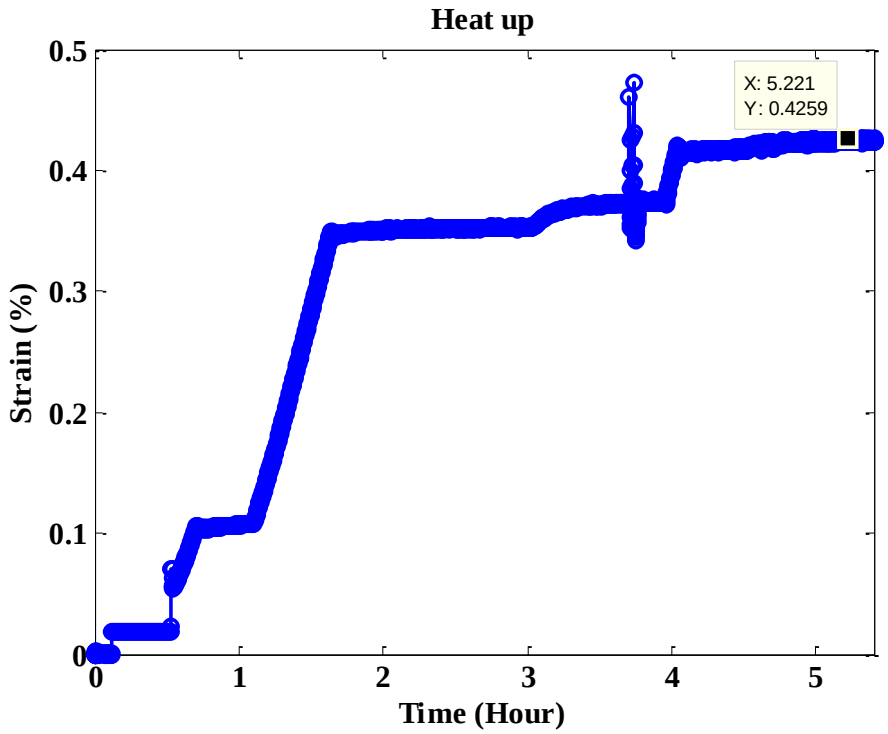

Figure 7. 8 Thermal strain measured at gauge center (during heat-up and temperature stabilization) of a typical 508 LAS specimen tensile test (conducted at ANL [18]).

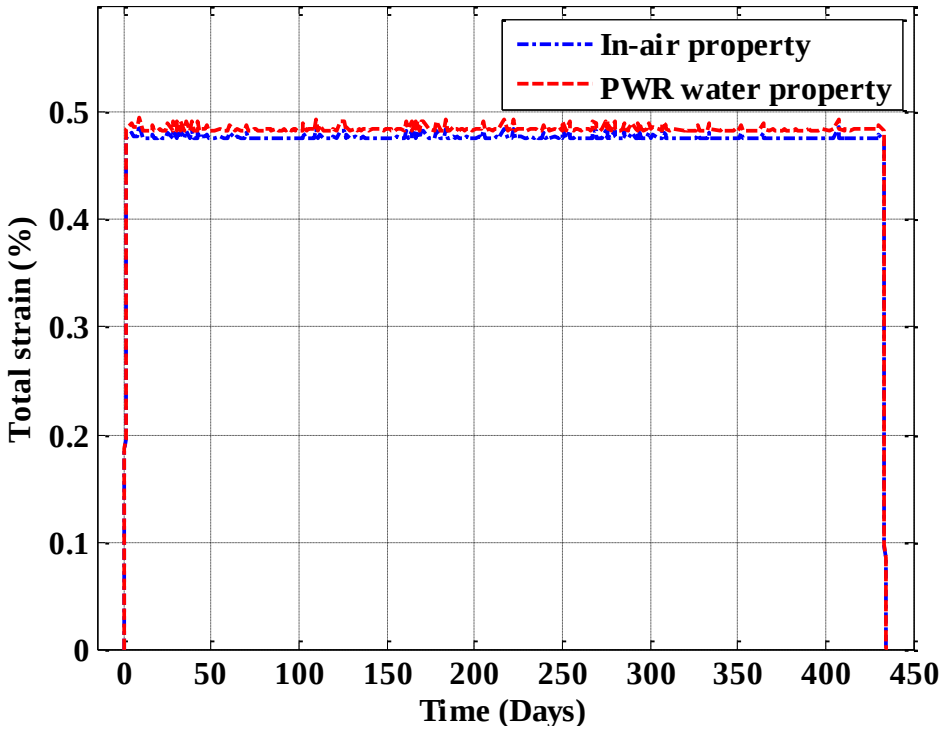

Figure 7. 9 Total strain histories estimated at a typical stressed element of CL nozzle for in-air and PWR water conditions.

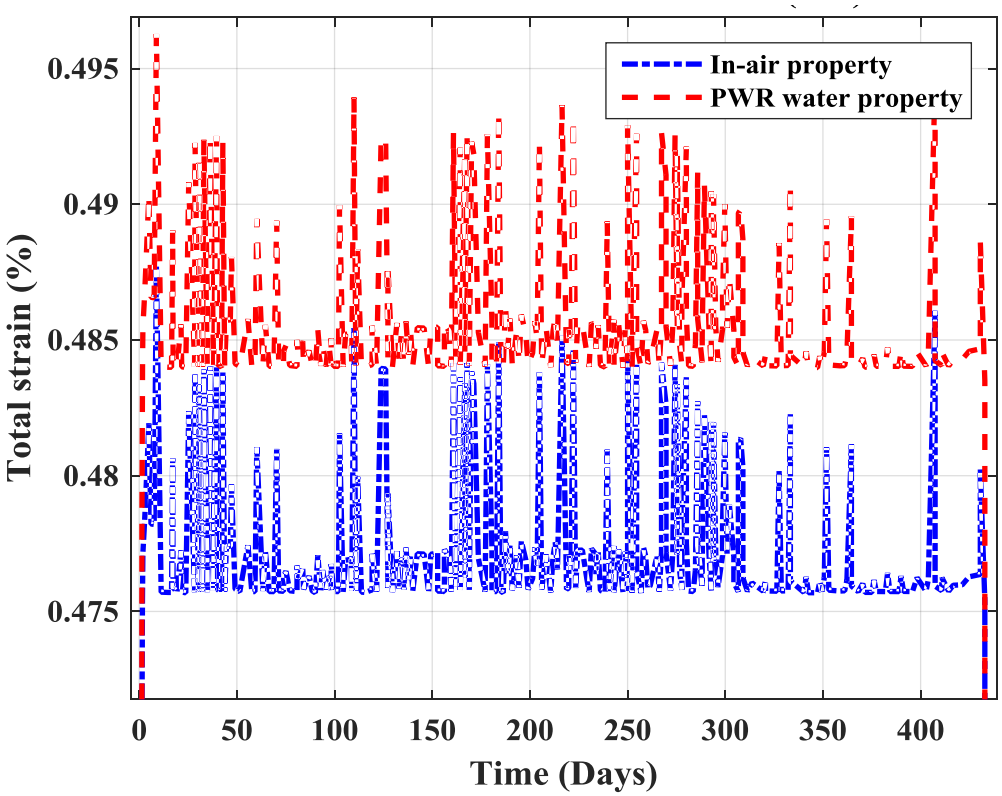

Figure 7. 10 Magnified form of Figure 7.9.

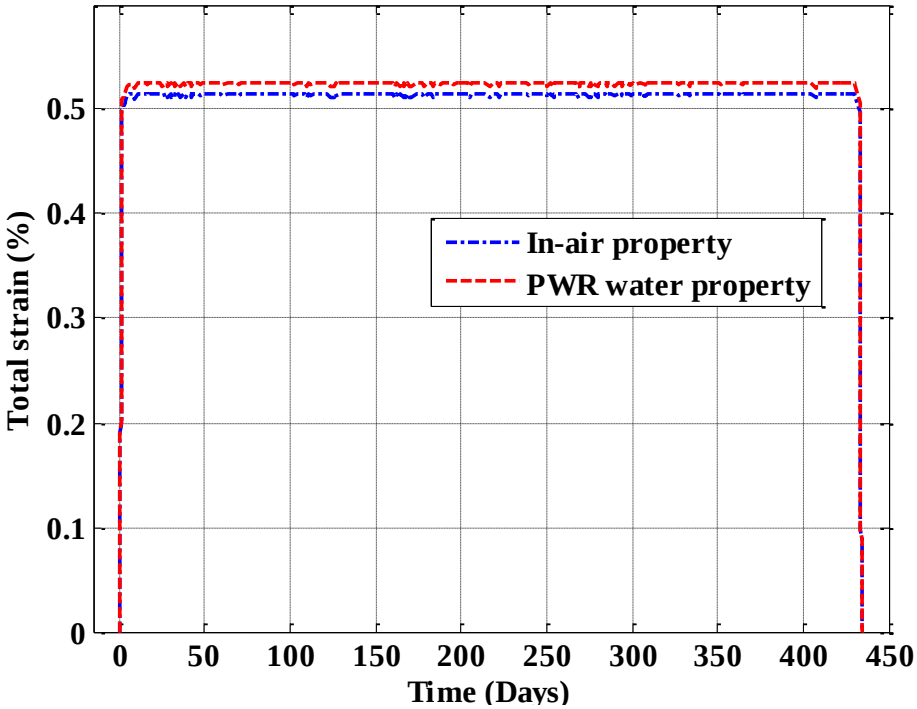

Figure 7. 11 Total strain histories estimated at a typical stressed element of HL nozzle for in-air and PWR water conditions.

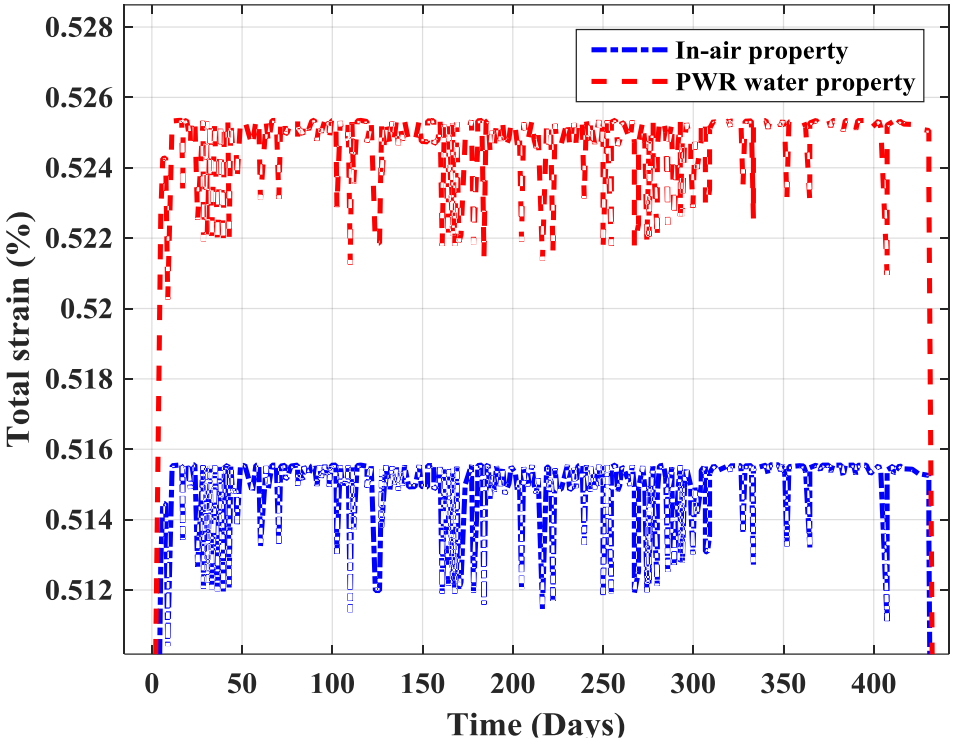

Figure 7. 12 Magnified form of Figure 7.11.

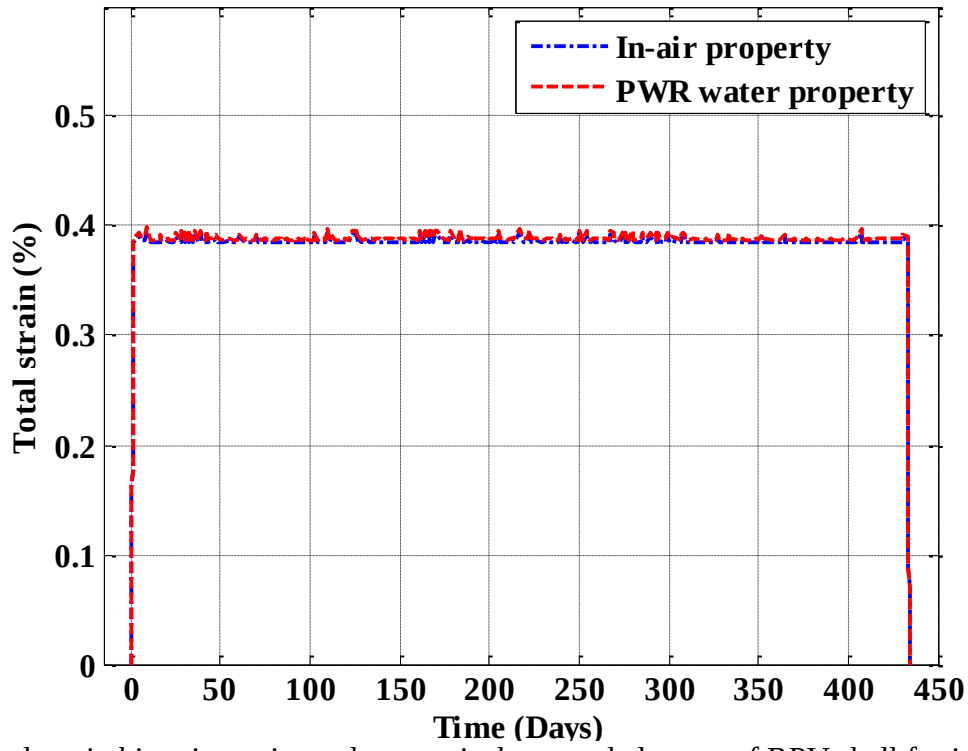

Figure 7. 13 Total strain histories estimated at a typical stressed element of RPV shell for in-air and PWR water conditions.

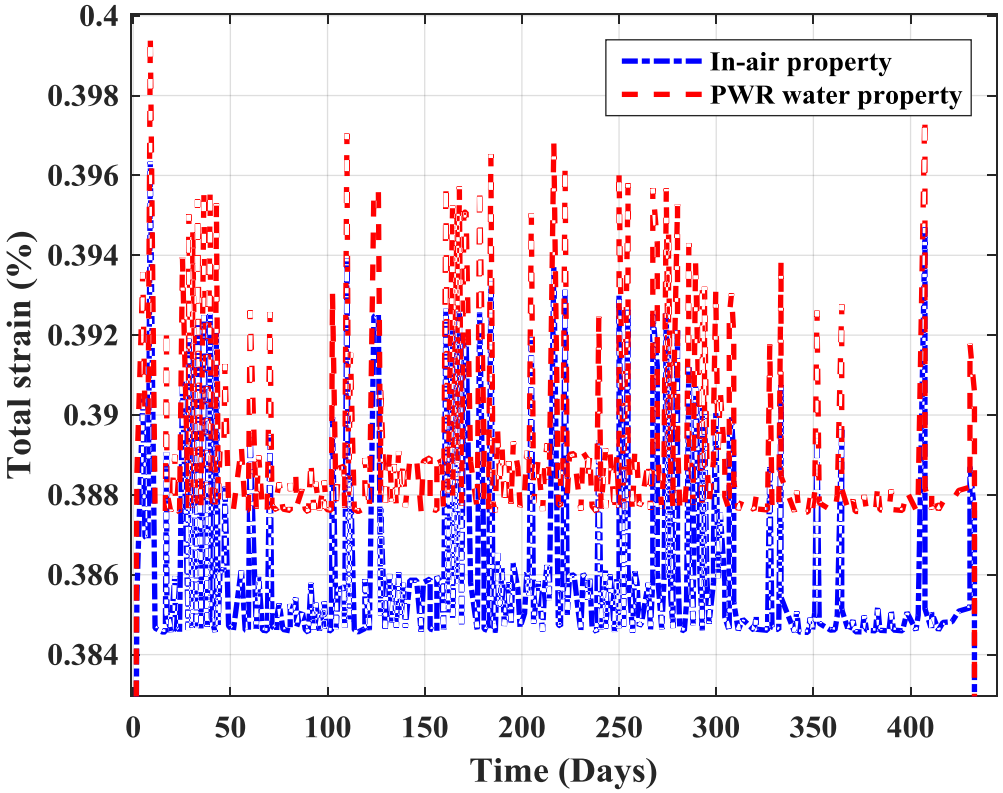

Figure 7. 14 Magnified form of Figure 7.13.

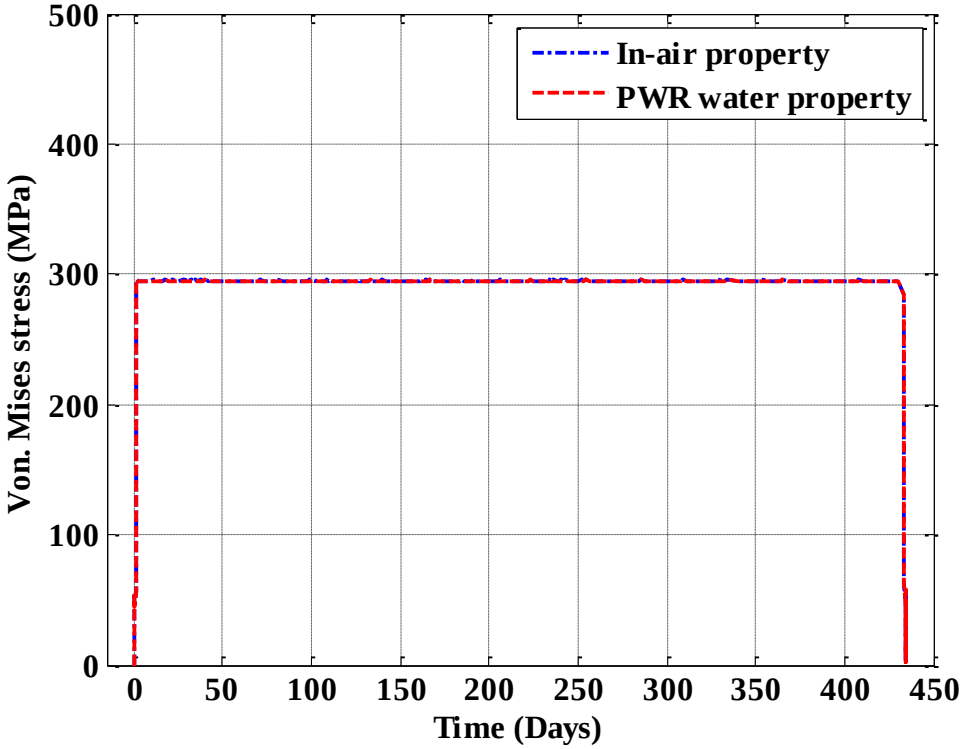

Figure 7. 15 Von-Mises histories estimated at a typical stressed element of CL nozzle for in-air and PWR water conditions.

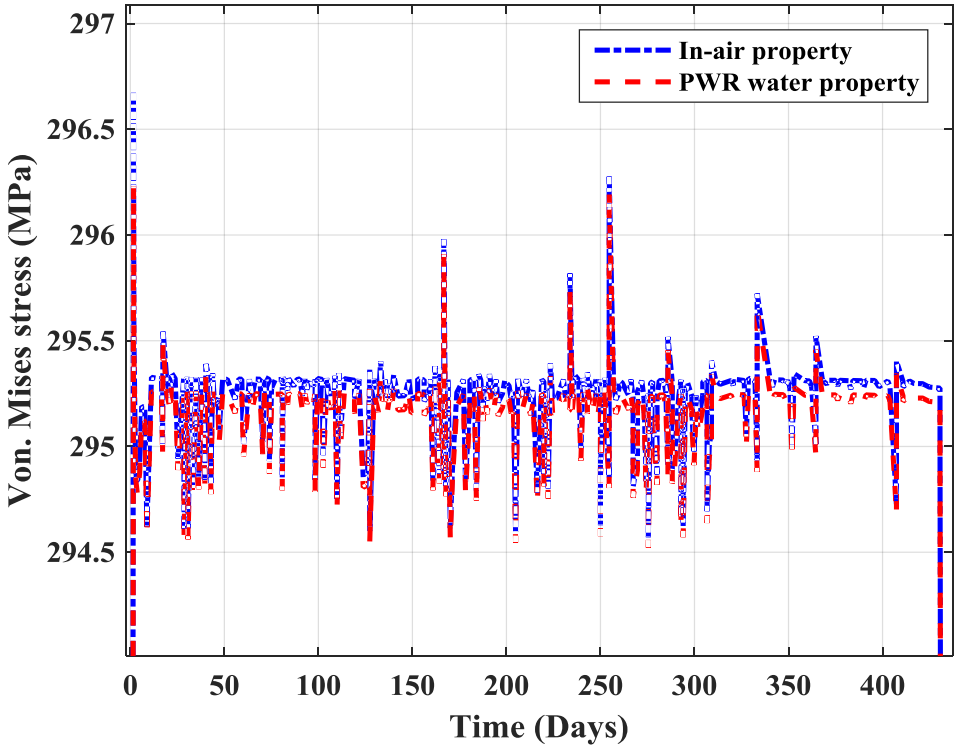

Figure 7. 16 Magnified form of Figure 7.15.

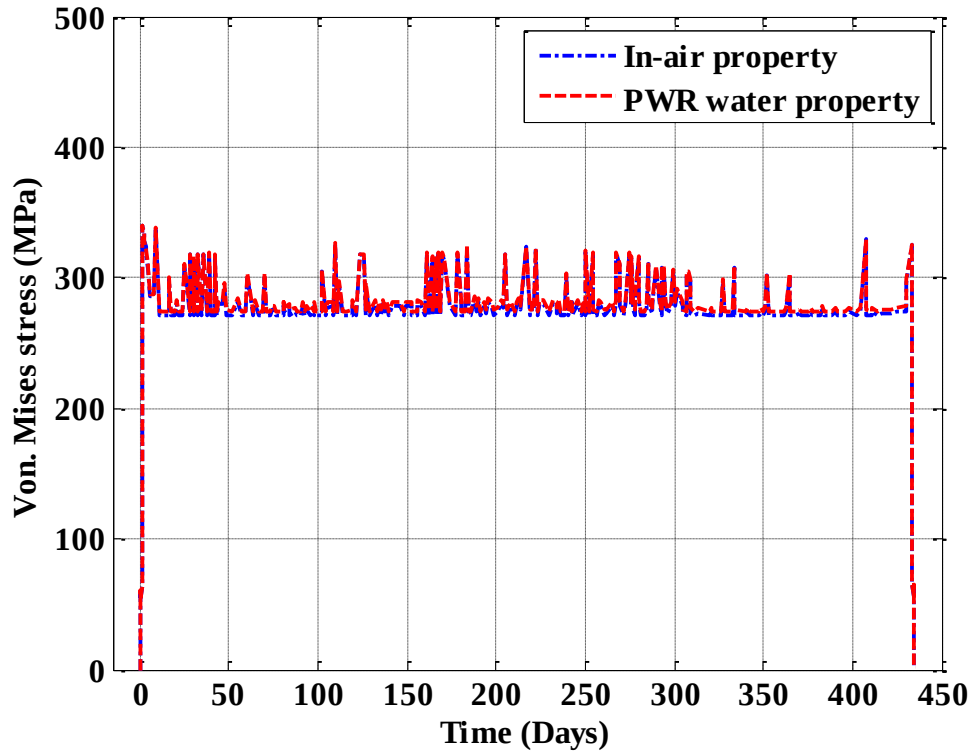

Figure 7. 17 Von-Mises histories estimated at a typical stressed element of HL nozzle for in-air and PWR water conditions.

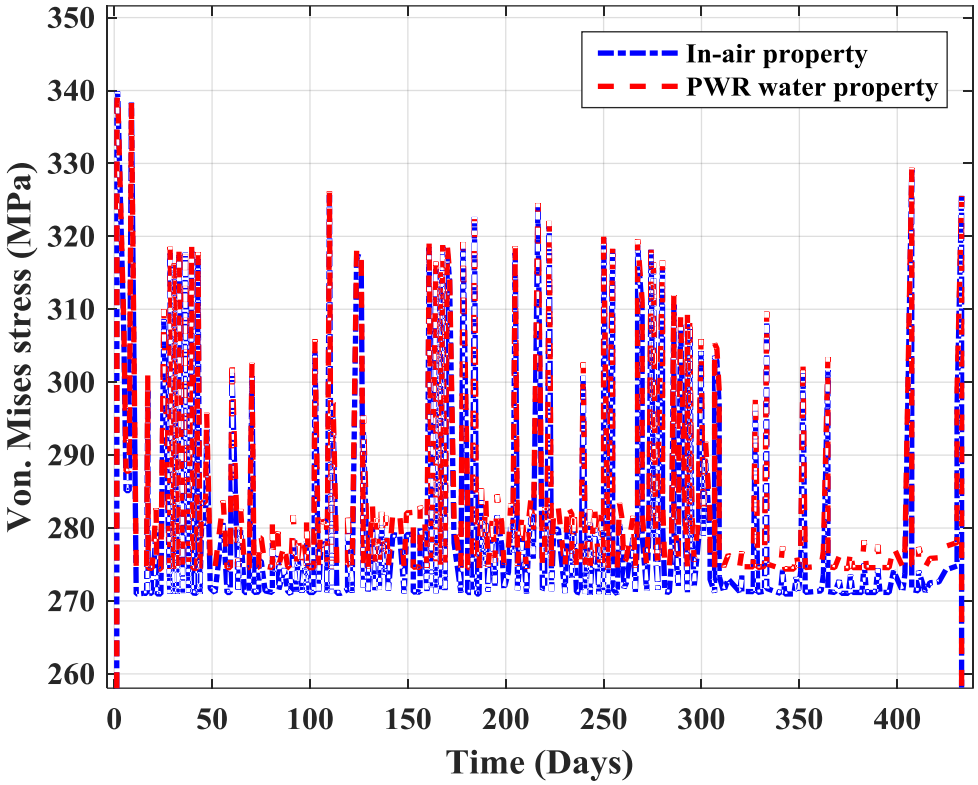

Figure 7. 18 Magnified form of Figure 7.17.

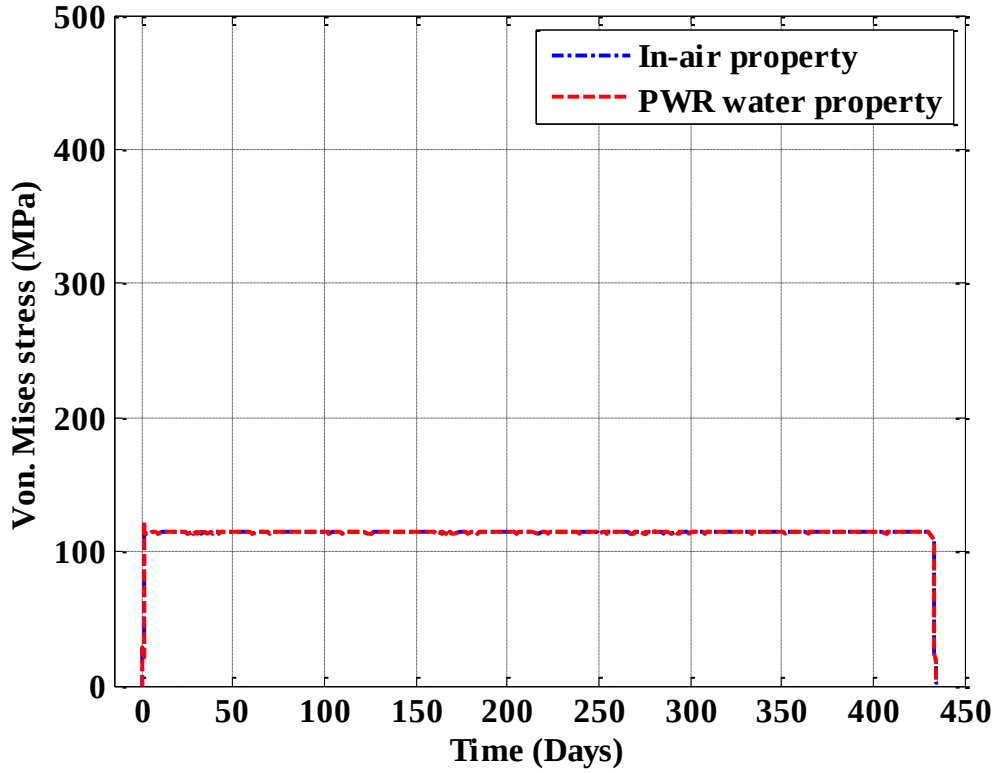

Figure 7. 19 Von-Mises histories estimated at a typical stressed element of RPV shell for in-air and PWR water conditions.

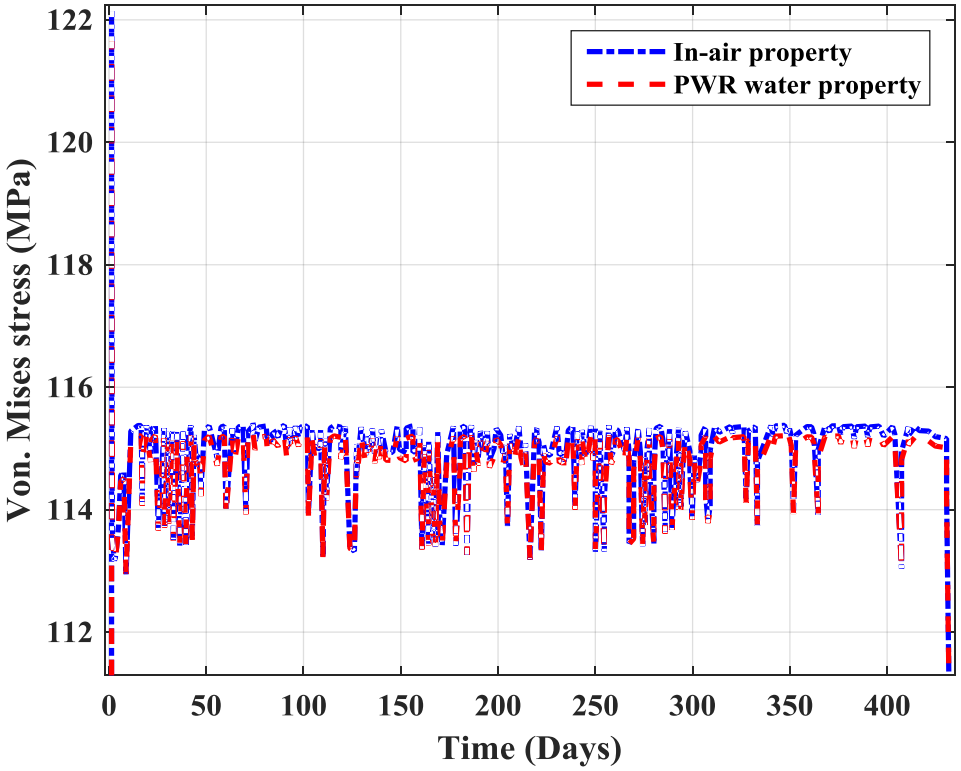

Figure 7. 20 Magnified form of Figure 7.19.

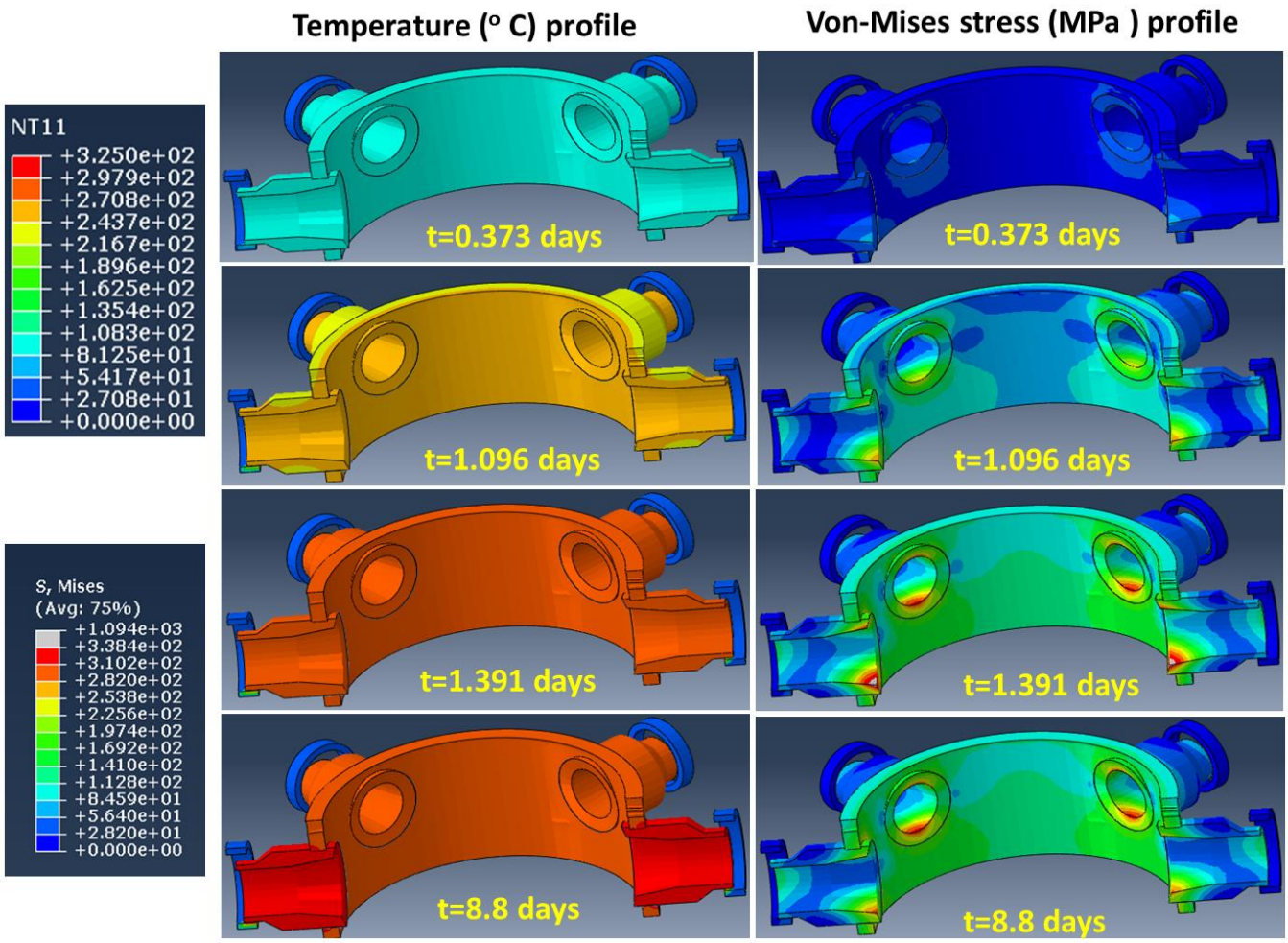

Figure 7. 21 Example temperature versus Von-Mises stress profile near the nozzle area (at different instances during heat-up and full power) obtained through case-1 FE simulation (in-air condition).

8 XFEM Modeling and Thermal-Mechanical Stress Analysis of RPV and Nozzles with Preexisting Cracks

A crack could develop in reactor components due to stress corrosion cracking or other environmental factors. For example in October 2000, during containment inspection after entering a refueling outage at V.C. Summer NPP, an axial through-wall crack along with a small circumferential crack was found in the first weld between the reactor vessel nozzle and the hot leg piping of the coolant system (RCS) [38]. The crack was approximately 3 feet from the reactor vessel. Based on Ultrasonic testing data, it was found that the axial crack initiated from the ID surface and became complete through-wall. Primary water stress corrosion cracking (PWSCC) was suspected to be the main mechanism behind this type of crack formation. In this section we discuss stress analysis results of the RPV with simulated preexisting cracks. Thermal-mechanical stress analyses under the grid load-following condition were performed to predict the stress-strain state of the RPV at stress hotspots. The stress analyses were performed for two different crack shapes and locations:

- Case 1 (axial crack): An axial crack approximately 50% through-wall was modeled for the HL nozzle (refer to Figure 8.1).
- Case 2 (circumferential crack): An 180^o circumferential crack was modeled for the HL nozzle (refer to Figure 8.2).

Both FE simulations were performed using elastic-plastic material properties interpolated/extrapolated by using the elastic-plastic material properties estimated from half-life (cycle = N/2) stress-strain data of RT-F23 (in-air, 22^{o}C) and EN-F20 (PWR water, 300 ^{o}C) tests. As discussed in the previous section on stress analysis models, for the FE model discussed in this section we used nodal temperature data from earlier heat transfer results. The temperature data considered from the heat transfer model that used the insulated boundary condition for the RPV OD surfaces (refer to Section 4.2.3). In addition to the nodal temperature as input, we modeled internal coolant water pressure using the time-dependent pressure boundary condition shown in Figure 3.8. The corresponding thermal-mechanical stress analysis results are presented here. For example, Figure 8.3 shows the case-1 (axial crack) level set function Φ contours (magnified by 100 times) at a full power condition (at time = 421.6 days). Note that Φ is the signed distance function, which gives displacement of the node from the crack face at a given time, and Φ=0 defines the crack face. This figure shows that the crack has not opened up. This is because the stress was not great enough to open and grow the crack further. Figure 8.4 shows the corresponding (at time = 421.6 days) stress contour near the nozzle area. Figure 8.5 shows the case-1 (axial crack) comparison of Von-Mises stress histories at the maximum stressed node in the left HL nozzle and the corresponding maximum stressed node in the right HL nozzle. Figure 8.6 shows the corresponding comparison of total strain histories. Figures 8.5 and 8.6 indicate that the presence of a crack could create larger stress/strain compared to the condition with no crack, as in the case of the right HL nozzle. Higher stress/strain could accelerate PWSCC. Particularly higher strain can lead to accumulation of plastic strain, which can help the growth of PWSCC. We have also plotted accumulated plastic strain at different instance of heat-up and cool-down (the instances are highlighted in Figure 8.7) procedures. The corresponding contour plots are shown in Figure 8.8. From this figure it can be seen that, itself during the heat-up process plastic strain was generated. For example at t=1.096 days (corresponding RCS heat-up temperature was 172.2 ^{o}C; refer Figure 8.7) the accumulated plastic strain magnitude is approximately 0.017%. Furthermore, Figure 8.8 indicates over the entire reactor fuel cycle (434.9 days) the plastic strain has grown to a magnitude of 0.079%. Note that in the base metal ASME code case N-47 [34, 39], specifies that the averaged through-the-thickness limit and linearized surface strain limits are 1% and 2%,

respectively. These limits are reduced by 50% for the weld metal. In this context if we assume linear accumulation of plastic strain and a maximum allowable total strain limit of 2% and with approximate estimated elastic strain of 0.525% (refer Figure 7.12) the total allowable plastic strain limit is 1.475%. Note that Figure 7.12 shows the total strain history in HL without the presence of any crack. It is found that, in the absence of preexisting crack the stress-strain state of HL mostly remain under elastic condition. Now with the presence of preexisting crack (case-1 axial crack) and with the assumption of maximum allowable plastic or inelastic limit of 1.475%, total number of remaining reactor cycle can be estimated as 18.6 (1.475/0.079). That means with the presence of a 50% through-wall crack in the HL nozzle the reactor still can survive approximately 18.6 reactor fuel cycles. However, the above estimation is assuming linear accumulation of plastic strain, requires more detailed analysis.

In addition to the above axial crack case, we performed thermal-mechanical stress analysis for case 2 (circumferential crack). Figure 8.9 shows the level set function Φ contours at the above-mentioned full power condition (at time = 421.6 days). Figure 8.10 show the corresponding (at time = 421.6 days) stress contours near of HL/CL nozzles and nearby RPV ID surfaces. Figure 8.11 shows the Von-Mises stress histories at the maximum stressed node in the left HL and the corresponding maximum stressed node in the right HL. Figure 8.12 shows the corresponding comparison of total strain. Figure 8.13 shows the contour plot of accumulated plastic strain at the end of reactor fuel cycle i.e. at 434.9 days. From the Figure 8.13 it can be seen that for circumferential crack case there is no plastic strain observed, that means over the entire fuel cycle even there was a crack, the CL nozzle (and other components such as other CL nozzles, HL nozzles and RPV) were mostly under elastic conditions. Also comparing Figure 8.11 (case 2: circumferential crack) with Figure 8.5 (case 1: axial crack), we found that the circumferential crack does not create much stress compared to the axial crack. This could be why a larger axial crack formed in the V.C. Summer NPP (as mentioned above) by cumulative growth of PWSCC along the axial direction.

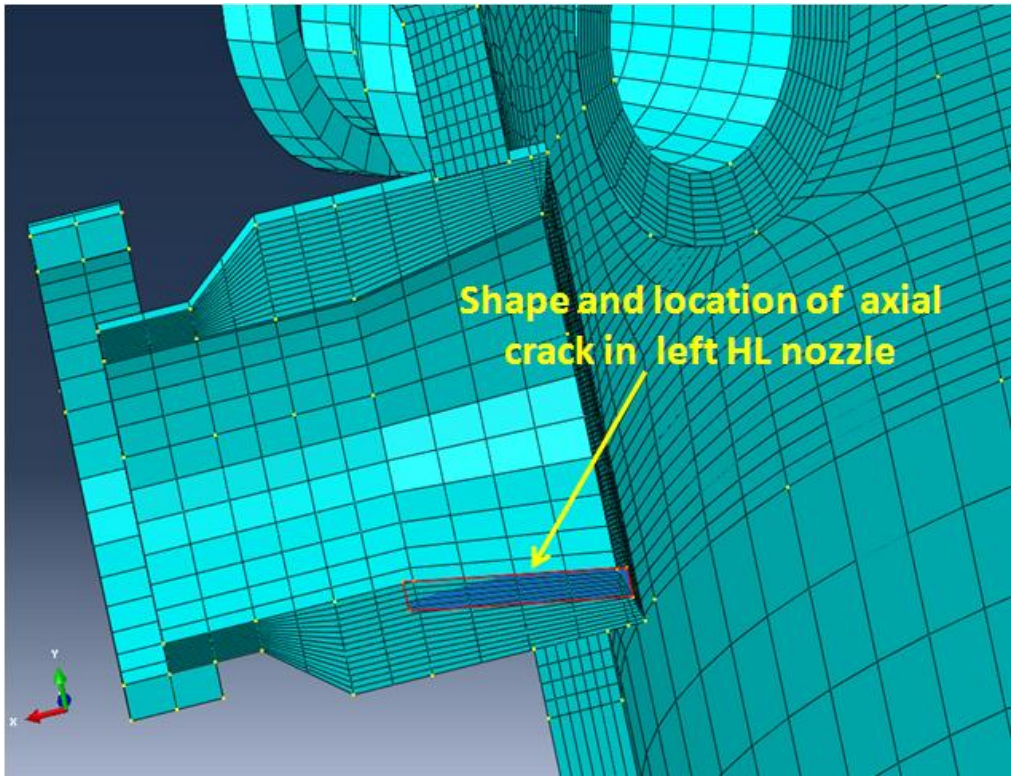

Figure 8.1 Shape and location of axial crack in left HL nozzle of RPV.

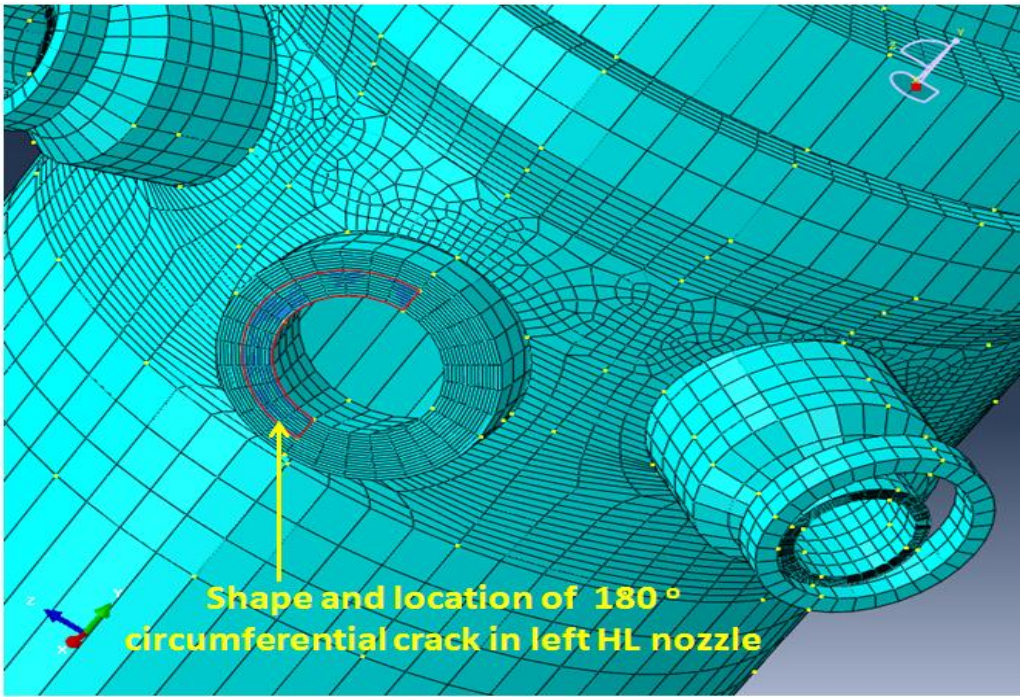

Figure 8.2 Shape and location of circumferential crack in left HL nozzle of RPV.

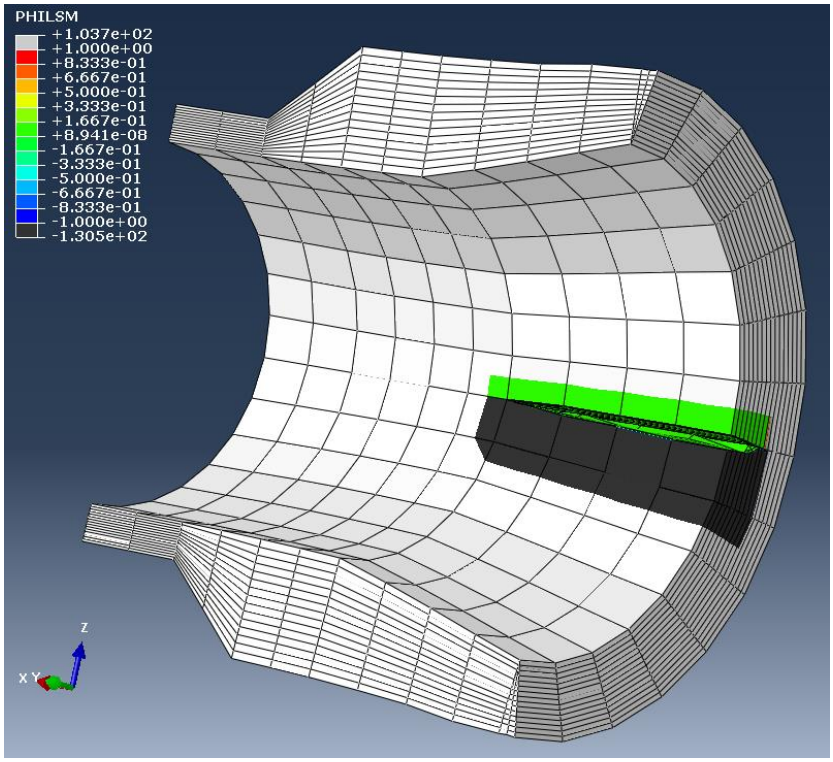

Figure 8. 3 Level set function (Φ) contour (magnification factor = 100) at a typical full power condition (at time = 421.6 days) for case 1 (axial crack).

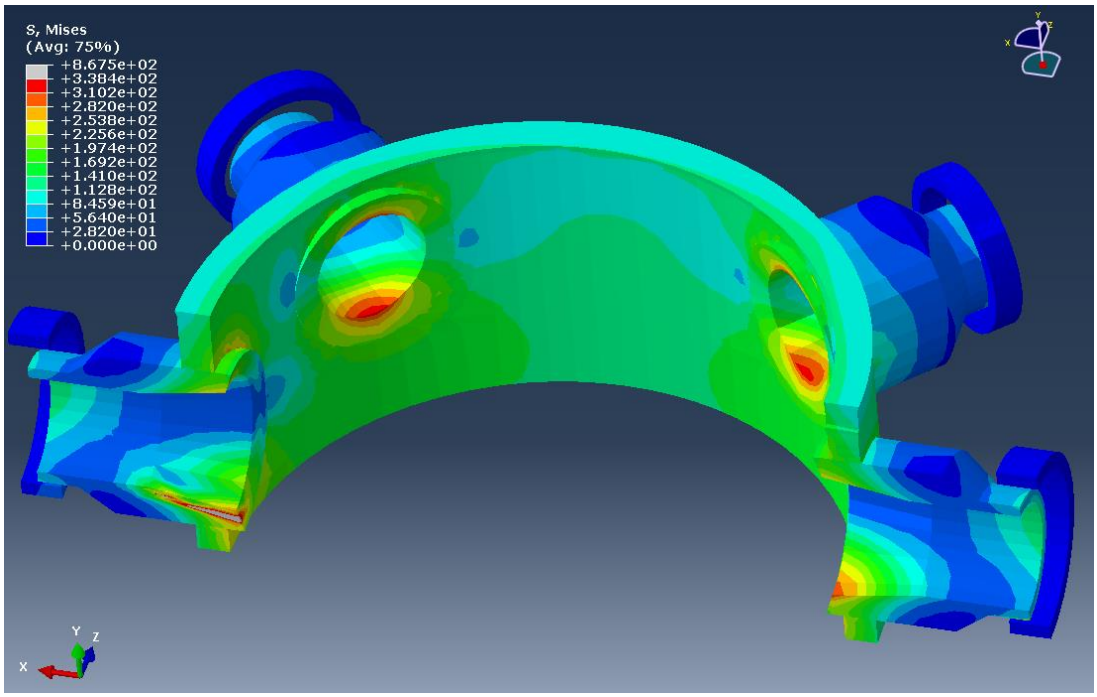

Figure 8. 4 Von-Mises stress contour at a typical full power condition (at time = 421.6 days) for case 1 (axial crack).

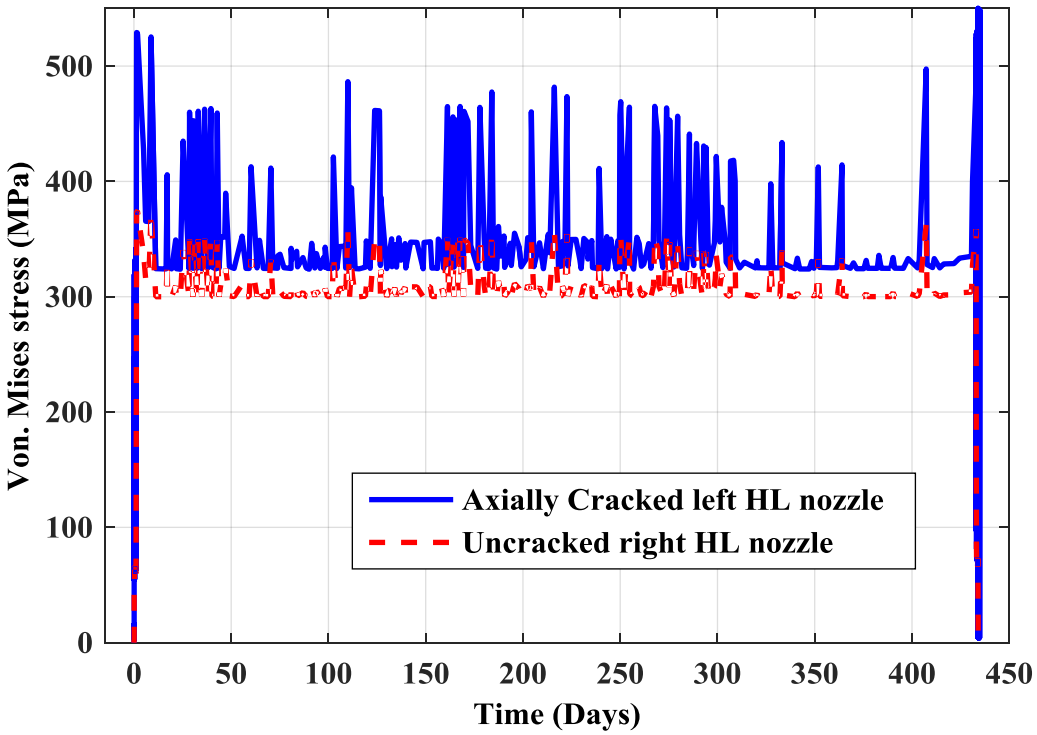

Figure 8. 5 Von-Mises stress histories at maximum stressed node in left HL and the corresponding maximum stressed node in right HL for case 1 (axial crack).

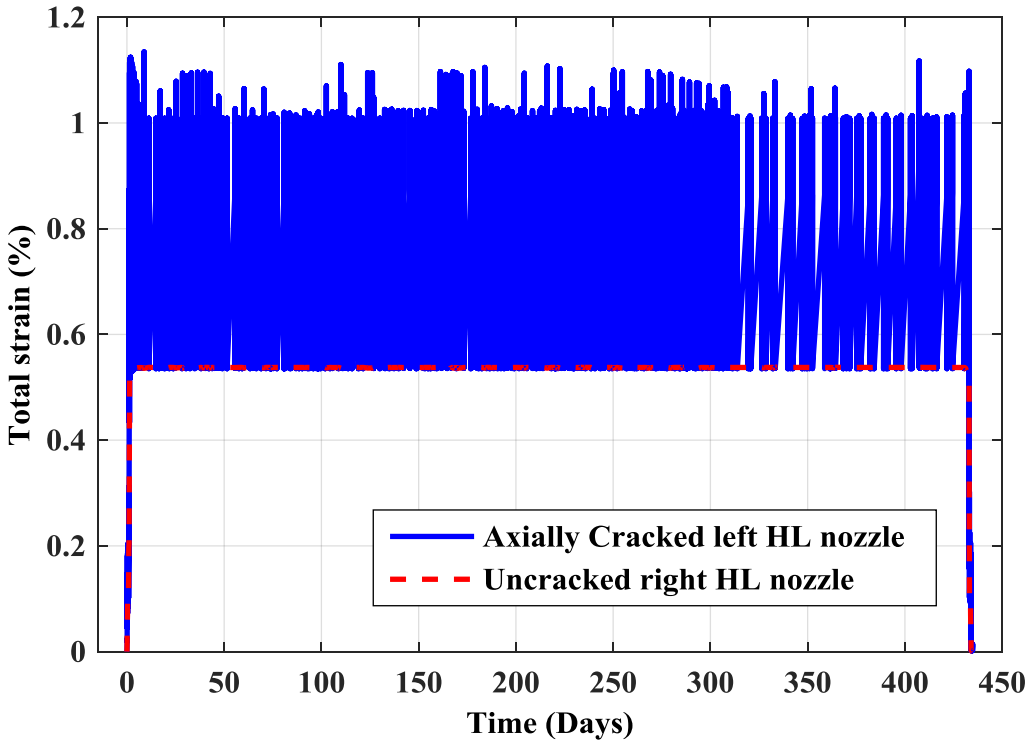

Figure 8. 6 Total strain histories at maximum stressed node in left HL and the corresponding maximum stressed node in right HL for case 1 (axial crack).

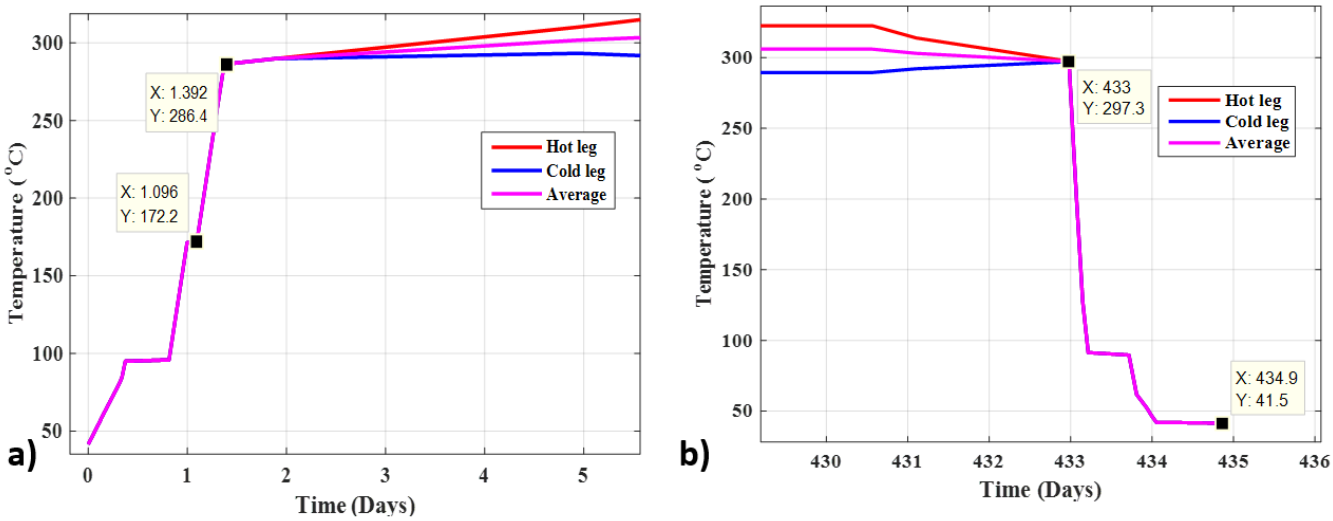

Figure 8. 7 Heat-up and cool-down temperature boundary condition showing different instance at which the magnitude of accumulated plastic strain contours are plotted and are shown in Figure 8.7.

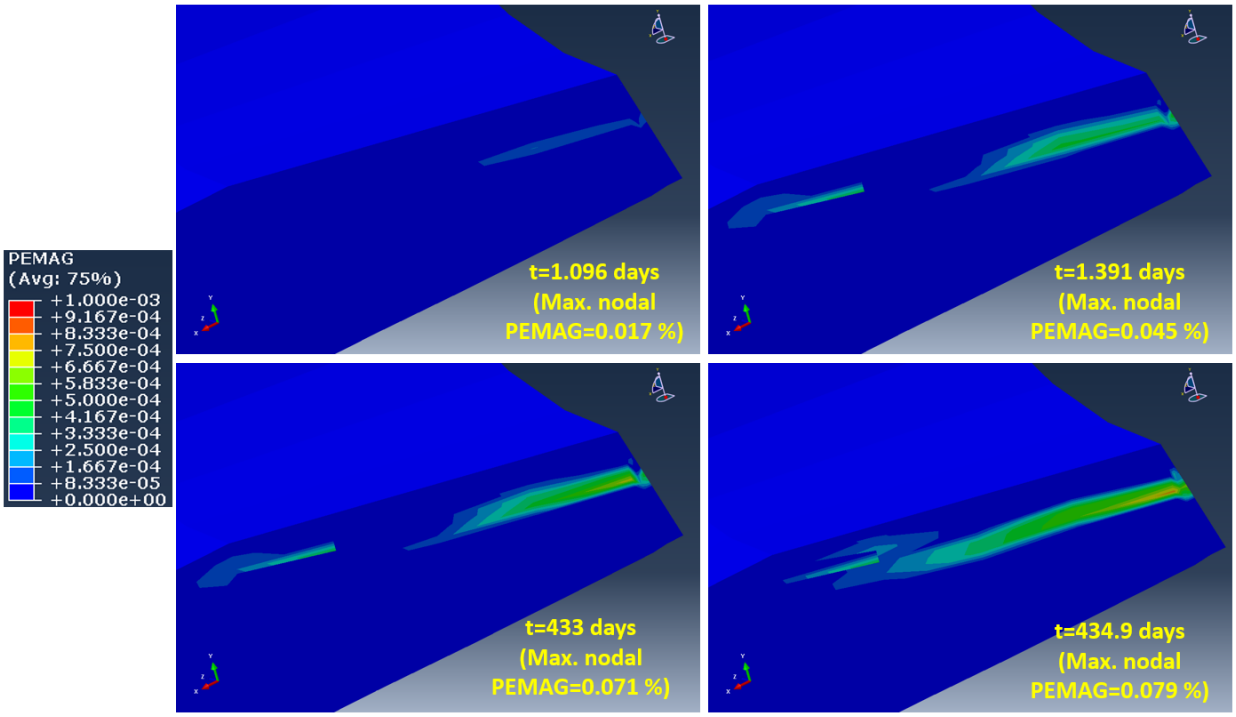

Figure 8. 8 Contour plots of accumulated plastic strain magnitude (PEMAG) in the cracked region of HL (right hand side of contours are towards the RPV ID surface). These contour plots are for case 1 (axial crack) and plotted at different instances shown in Figure 8.6.

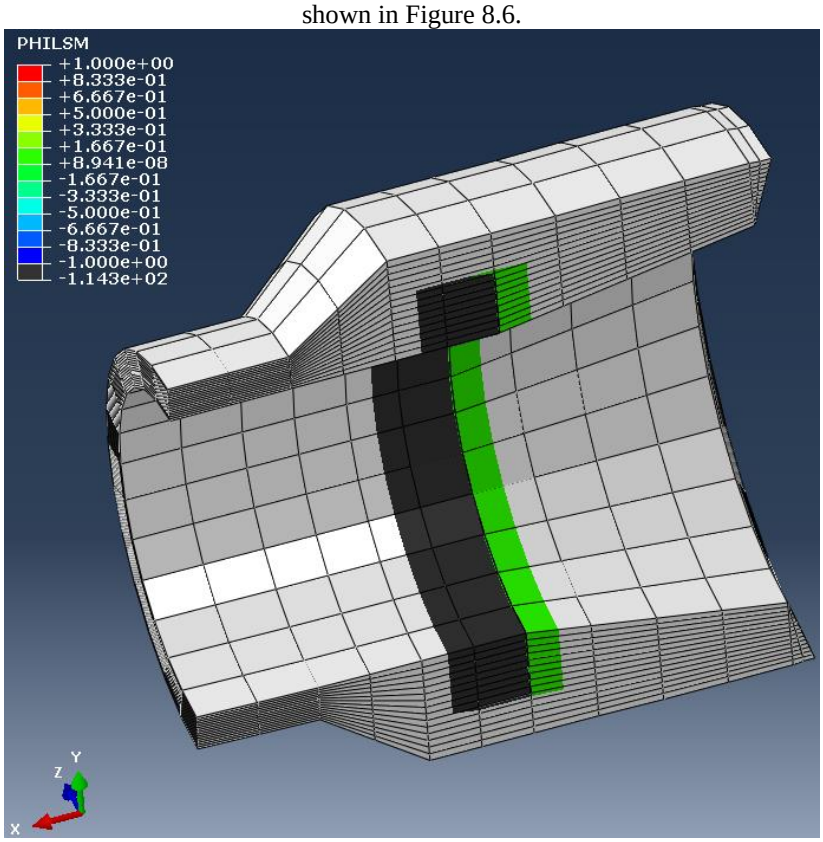

Figure 8. 9 Level set function (Φ) contour (magnification factor = 100) at a typical full power condition (at time = 421.6 days) for case 2 (circumferential crack).

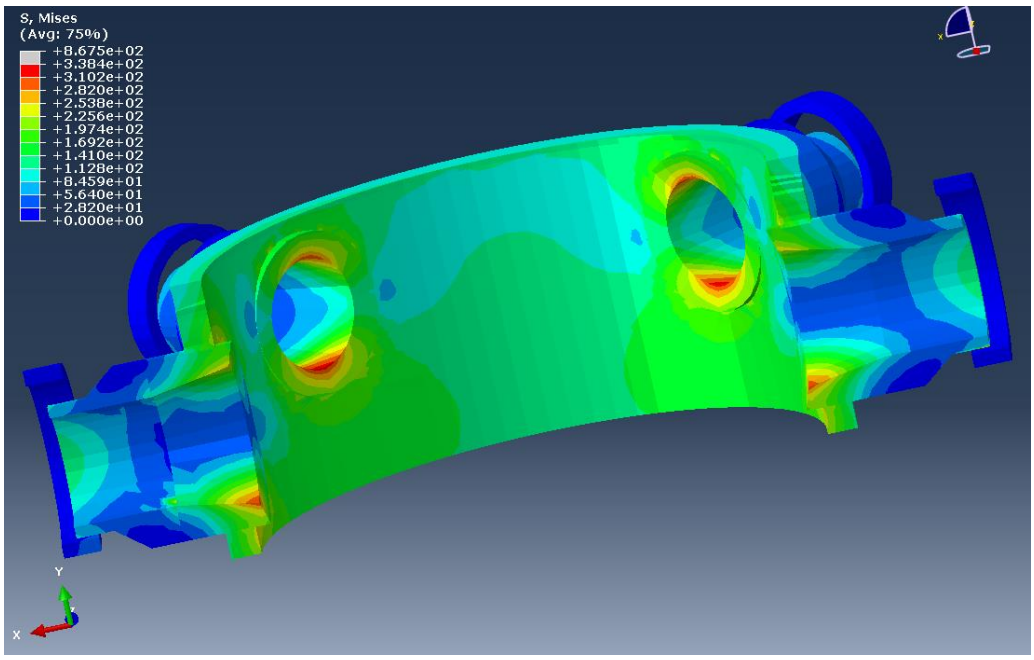

Figure 8. 10 Von Mises stress contour at a typical full power condition (at time = 421.6 days) for case 2 (circumferential crack).

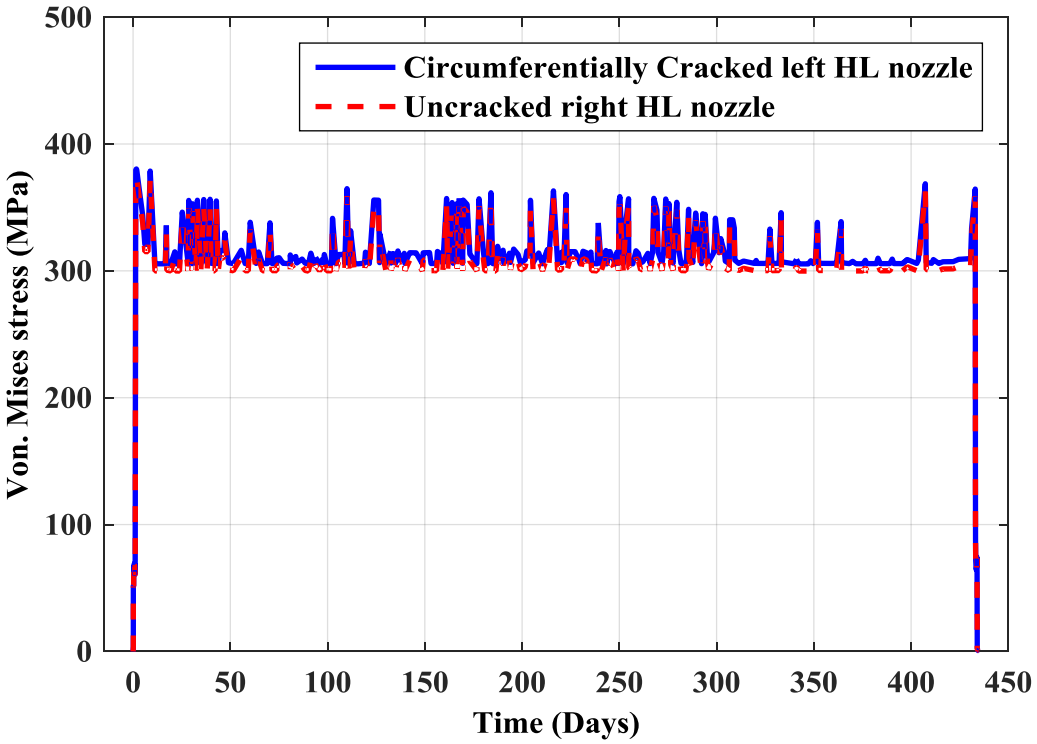

Figure 8. 11 Von-Mises stress histories at maximum stressed node in left HL and the corresponding maximum stressed node in right HL for case 2 (circumferential crack).

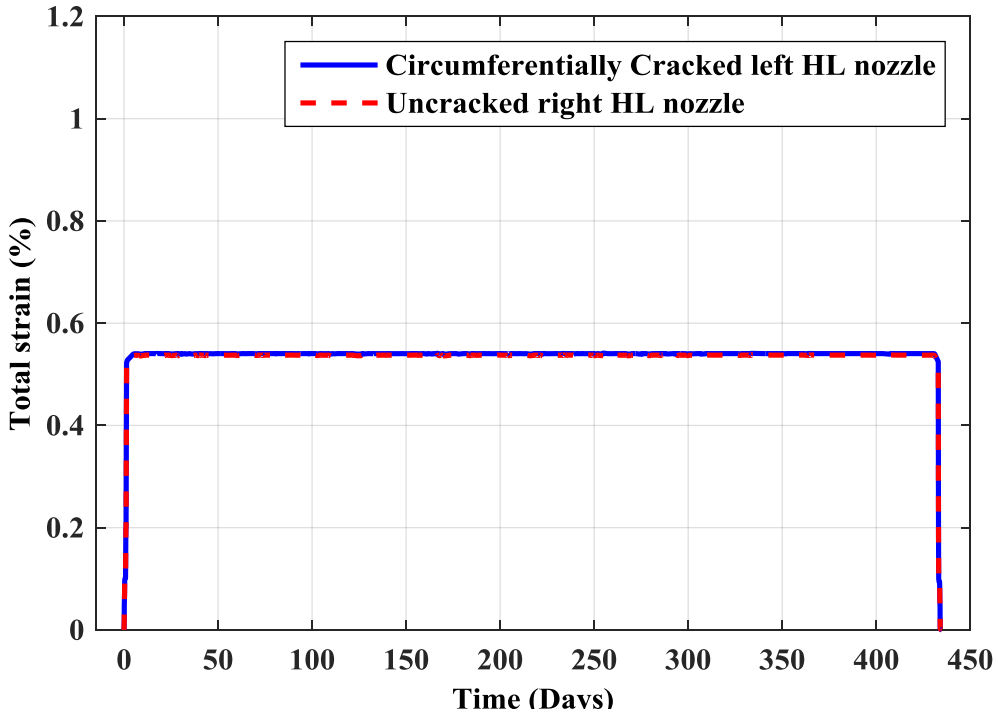

Figure 8. 12 Total strain histories at maximum stressed node in left HL and the corresponding maximum stressed node in right HL for case 2 (circumferential crack).

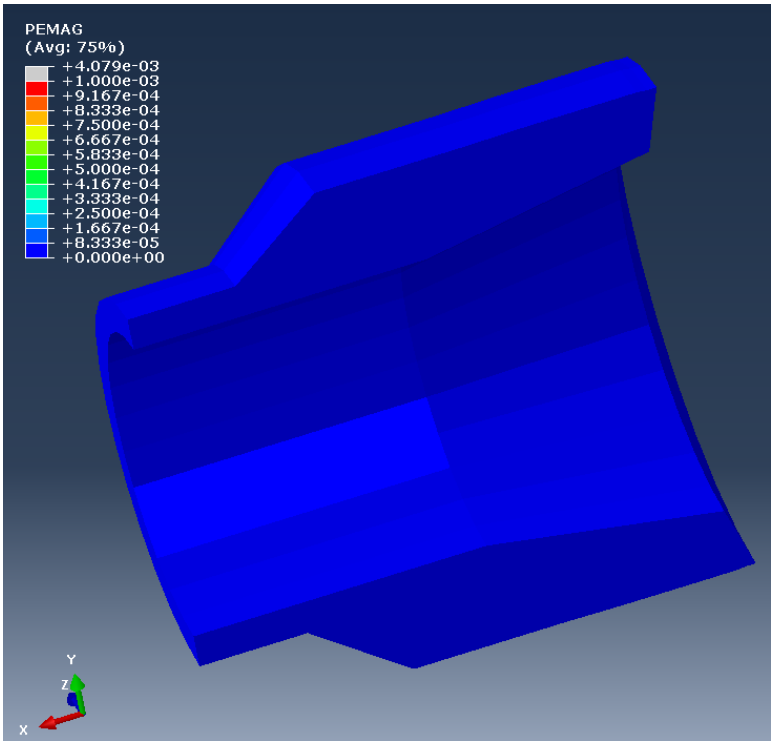

Figure 8. 13 Contour plot of accumulated plastic strain magnitude (PEMAG) in the cracked region of HL at end of simulation (at 434.9 days).

9 Summary and Future Study

This report presents the following:

1. Results from heat transfer analysis of the RPV under heat-up, cool-down, and grid load-following power operation.
2. Results from thermal-mechanical stress analysis of the RPV and nozzles with/without preexisting crack under heat-up, cool-down, and grid load-following power operation.
3. Results from the stress analysis validation model for ANL-tested tensile and fatigue specimens.

From the thermal-mechanical stress analysis of RPV and its nozzle we found that under grid load following condition there is a large variation in stress and strain in HL nozzle. The stress-strain variation in HL nozzle even further amplified if there is a preexisting crack. From the model results it is found that the stress-strain states are significantly higher in case of axial crack than circumferential crack. This could be why a larger axial crack formed in the V.C. Summer NPP, as mentioned earlier. The stress-strain state under grid load following condition are more realistic compared to the stress-strain state estimated assuming simplified transients. Also from the preliminary calculation we estimated that with the presence of a 50% through-wall crack in the HL nozzle, the reactor still can survive approximately 18.6 reactor fuel cycles. However, the above estimation is only representative and based on linear accumulation of plastic strain. For more accurate estimation of fatigue life it requires more detailed analysis and is one of our future work.

Suggested future work includes the following:

1. Include RPV insulation and its gap between the RPV outer surfaces in the heat transfer analysis model for more accurate estimation of the across-thickness temperature profile.
2. Perform thermal-mechanical stress analysis with other crack sizes and shapes.
3. Perform fatigue tests (under both in-air and PWR water conditions) using the random stress history in the grid-following mode and then compare the corresponding experimentally observed strains with FE-estimated strains and vice versa.
4. Include more reactor loading conditions (e.g., pressure, pressurized thermal shock conditions, etc.) in stress analysis.
5. Perform weld modeling using similar and dissimilar metal welds to the RPV nozzle safe ends.

References

1) Chu, S., and A. Majumdar. "Opportunities and challenges for a sustainable energy future." *Nature* 488, no. 7411 (2012): 294-303.
2) Lokhov, A. "Load-following with nuclear power plants." *NEA News* 29, no. 2 (2011): 18 (https://www.oecd-nea.org/nea-news/2011/29-2/nea-news-29-2-load-following-e.pdf).
3) Lokhov, A. *Technical and Economic Aspects of Load Following with Nuclear Power Plants: Nuclear Development Division*. OECD Nuclear Energy Agency, Paris, France (2011).
4) Bruynooghe, C., A. Eriksson, and G. Fulli G. *Load-following Operating Mode at Nuclear Power Plants (NPPs) and Incidence on Operation and Maintenance (O&M) Costs: Compatibility with Wind Power Variability*. EUR 24583 EN, Joint Research Centre, Institute for Energy , Petten, the Netherlands (2010).
5) International Atomic Energy Agency. "Load following EDF experience feedback." IAEA Technical Meeting: Load Following, https://www.iaea.org/NuclearPower/Downloadable/Meetings/2013/2013-09-04-09-06-TM-NPE/8.feutry_france.pdf, Paris, France, September 4-6, (2013).
6) Savolainen, Aleksi. "The role of nuclear and other conventional power plants in the flexible energy system.", Master's thesis, Lappeenranta University of Technology, http://www.doria.fi/bitstream/handle/10024/118575/Masters_thesis_Aleksi_Savolainen.pdf?sequence=2 (2015).
7) Ablay, Günyaz. "A modeling and control approach to advanced nuclear power plants with gas turbines." *Energy Conversion and Management* 76 (2013): 899-909.
8) Foley, A. M., B.P. Ó. Gallachóir, J. Hur, R. Baldick, and E. J. McKeogh. "A strategic review of electricity systems models." *Energy* 35, no. 12 (2010): 4522-4530.
9) Jaleeli, N., L. S. VanSlyck, D. N. Ewart, L. H. Fink, and A. G. Hoffmann, "Financial analysis of hydro-power load following and improvement of system operational flexibility through wind farm participation in AG." https://www.bpa.gov/Doing%20Business/TechnologyInnovation/ConferencesReservoirSystemModeling/7_1_Antonishen.pdf.
10) Ingersoll, D.T., C. Colbert, Z. Houghton, R. Snuggerud, J. W. Gaston, and M. Empey. "Can nuclear power and renewables be friends?" Proceedings of ICAPP 2015, Paper 15555, Nice, France, May 3-6, 2015Paper 15555 (http://www.nuscalepower.com/images/our_technology/NuScale-Integration-with-Renewables_ICAPP15.pdf).
11) Mohanty, S., W. Soppet, S. Majumdar, and K. Natesan. *System-Level Heat Transfer Analysis, Thermal- Mechanical Cyclic Stress Analysis, and Environmental Fatigue Modeling of a Two-Loop Pressurized Water Reactor. A Preliminary Study*. Argonne National Laboratory Report ANL/LWRS-15/01 (2015) (doi:10.2172/1179020, http://www.osti.gov/scitech/servlets/purl/1179020).
12) Mohanty, S., W. K. Soppet, S. Majumdar, and K. Natesan. "Full-scale 3-D finite element modeling of a two-loop pressurized water reactor for heat transfer, thermal–mechanical cyclic stress analysis, and environmental fatigue life estimation." *Nuclear Engineering and Design* 295 (2015): 374-387.
13) Wilhelm, P., J. Rudolph, and P. Steinmann. "Study on fatigue analysis for operational load histories." 39th MPA-Seminar,

http://www.iaea.org/inis/collection/NCLCollectionStore/_Public/45/107/45107459.pdf (October 2013), Stuttgart.

14) Bergholz, S., J. Rudolph, F. Bruckmueller, B. Heinz, and B. Jouan. "Automatic fatigue monitoring based on real loads: Live demonstration." 38th MPA Demonstration, Stuttgart, Germany, October 1-2, 2012 (http://www.iaea.org/inis/collection/NCLCollectionStore/_Public/46/001/46001472.pdf).
15) Rudolph, J., and S. Bergholz. "The AREVA integrated and sustainable concept of fatigue design, monitoring and re-assessment." Proceedings of ASME 2008 Pressure Vessels and Piping Conference, Paper No. PVP2008-61897 (2008).
16) Shah, V. N., and P.E. MacDonald. *Aging and Life Extension of Major Light Water Reactor Components.* Elsevier Science (1993).
17) Chopra, O., and G. Stevens. *Effect of LWR Coolant Environments on the Fatigue Life of Reactor Materials*. U.S. Nuclear Regulatory Commission Report No. NUREG/CR-6909, Revision 1 (2014).
18) Mohanty, S., W. Soppet, S. Majumdar, and K. Natesan. *Tensile and Fatigue Testing and Material Hardening Model Development for 508 LAS Base Metal and 316 SS Similar Metal Weld under In-Air and PWR Primary Loop Water Conditions*. Argonne National Laboratory Report ANL/LWRS-15/02 (2015) (doi:10.2172/1224989; http://www.osti.gov/scitech/servlets/purl/1224989).
19) Mohanty, S., W. Soppet, S. Majumdar, and K. Natesan. *Environmental Effect on Evolutionary Cyclic Plasticity Material Parameters of 316 Stainless Steel: An Experimental & Material Modeling Approach.* Argonne National Laboratory Report ANL/LWRS-14/01 (2014) (doi:10.2172/1168233; http://www.osti.gov/scitech/servlets/purl/1168233).
20) Dassault Systèmes. "ABAQUS unified FEA: Complete solutions for realistic simulation." http://www.3ds.com/products-services/simulia/products/abaqus (2014).
21) Schulz, T. L. "Westinghouse AP1000 advanced passive plant." *Nuclear Engineering and Design* 236, no. 14 (2006): 1547-1557.
22) Cummins, W. E., M. M. Corletti, and T.L. Schulz. "Westinghouse AP1000 Advanced Passive Plant." *Proceedings of ICAPP*, Vol. 3, pp. 4-7 (2003).
23) Westinghouse Electric. *Westinghouse AP600 Design Control Document*. US-NRC Publication, ML003691016, http://pbadupws.nrc.gov/docs/ML0036/ML003691016.html (2000).
24) Westinghouse Electric. *Westinghouse AP1000 Design Control Document*. US-NRC Publication, ML11171A500, http://pbadupws.nrc.gov/docs/ML1117/ML11171A500.html (2011).
25) Cooke, C., and H. Spann. "Reactor vessel and reactor vessel internals segmentation at Zion Nuclear Power Station–13230." Proceedings of WM2013 Conference, Phoenix, Arizona, February 24 -28, 2013 (http://www.wmsym.org/archives/2013/papers/13230.pdf).
26) Westinghouse Electric. *Westinghouse Technology Manual*. Chapter 17, http://pbadupws.nrc.gov/docs/ML0230/ML023040268.pdf.
27) Gamble, R. "Evaluation of pressure-temperature limits for normal RPV startup and shutdown. EPRI-NRC Public Meeting, Rockville, MD, August 28, 2012 ((http://pbadupws.nrc.gov/docs/ML1224/ML12243A266.pdf).
28) Betova, I., M. Bojinov, and T. Saario. *Start-up and Shut-down Water Chemistries in Pressurized Water Reactors*. Technical Research Centre of Finland, Report No. VTT-R-00699-12 (2012) (http://www.vtt.fi/inf/julkaisut/muut/2012/VTT-R-00699-12.pdf).

29) Sengers, J. V., J. T. R. Watson, R. S. Basu, B. Kamgar-Parsi, and R. C. Hendricks. "Representative equations for the thermal conductivity of water substance." *Journal of Physical and Chemical Reference Data* 13, no. 3 (1984): 893-933.
30) Shan, J., B. Zhang, J. Gou, and L. Cao, L. "Subchannel analysis, CFD modeling and verifications, CHF experiments and benchmarking." In *Science and Technology of Nuclear Installations*." Article ID 209747, Hindawi Publishing Corporation (2014).
31) Westinghouse Electric. *Westinghouse Technology Manual*, Section 5.4, "Containment temperature, pressure, and combustible gas control systems" (http://pbadupws.nrc.gov/docs/ML1122/ML11223A222.pdf).
32) International Atomic Energy Agency. *Natural Circulation in Water Cooled Nuclear Power Plants Phenomena, Models and Methodology for System Reliability Assessments*. International Atomic Energy Agency Report ISEA-TECHDOC-1474 (2005).
33) Gray, M. A., & Verlinich, M. M. (2012). Guidelines for Addressing Environmental Effects in Fatigue Usage Calculations. Electric Power Research Institute Report EPRI-1025823.
34) American Society of Mechanical Engineers (2010). ASME Boiler and Pressure Vessel Code, section III.
35) Mohanty, S., W. Soppet, and S. Majumdar. *Report on Assessment of Environmentally Assisted Fatigue for LWR Extended Service Conditions*. Argonne National Laboratory Report ANL/LWRS/13/01 (2013) (http://www.ipd.anl.gov/anlpubs/2013/04/76411.pdf).
36) Reinhardt, L., J.A. Cordes, and D. Geissler. "Using co-simulation to extend the usage of XFEM." Proceedings of SIMULIA Customer Conference, 2011.
37) Han, D.-J., and S.-P. Park. "Evaluation of fracture toughness of pressure vessel steel using charpy impact test specimens." *Nuclear Engineering and Technology* 19, no. 1 (1987): 1-9.
38) U.S. Nuclear Regulatory Commission. "Crack in weld area of reactor coolant system hot leg piping at V. C. Summer." U.S. NRC Letter Report, Information Notice 2000-017, 2000; Supplement 1, 2000; Supplement 2, 2001. (http://pbadupws.nrc.gov/docs/ML0105/ML010570353.pdf).
39) Dhalla, A. K. "A procedure to evaluate structural adequacy of piping system in creep range." *Benchmark Problem Studies and Piping System at Elevated Temperature* (1982): 47-59 (http://www.iaea.org/inis/collection/NCLCollectionStore/_Public/14/720/14720555.pdf) .

This page intentionally left blank

Nuclear Engineering Division
Argonne National Laboratory
9700 South Cass Avenue, Bldg. 208
Argonne, IL 60439

www.anl.gov

Argonne
National
Laboratory is a U.S. Department of Energy
laboratory managed by UChicago Argonne, LLC